Ore Geology Reviews 122 (2020) 103446

Contents lists available at ScienceDirect

Ore Geology Reviews

journal homepage: www.elsevier.com/locate/oregeorev

Multistage pyrites in the Nibao disseminated gold deposit, southwestern Guizhou Province, China: Insights into the origin of Au from textures, in situ trace elements, and sulfur isotope analyses

Dong-Tian Wei[a,b,c], Yong Xia[b,*], Daniel D. Gregory[c,d], Jeffrey A. Steadman[c], Qin-Ping Tan[b], Zhuo-Jun Xie[b], Xi-jun Liu[a]

[a] Guangxi Key Laboratory of Exploration for Hidden Metallic Ore Deposits, College of Earth Sciences, Guilin University of Technology, Guilin 541006, China
[b] State Key Laboratory of Ore Deposit Geochemistry, Institute of Geochemistry, Chinese Academy of Sciences, Guiyang 550002, China
[c] Centre for Ore Deposit and Earth Sciences, University of Tasmania, Private Bag 79, Tasmania 7001, Australia
[d] Department of Earth Sciences, University of Toronto, Earth Sciences Centre, 22 Russell Street, Toronto, Ontario M5S 3B1, Canada

ARTICLE INFO

Keywords:
Pyrite sulfur isotope
Pyrite trace element
Nibao gold deposit
Disseminated gold deposit

ABSTRACT

Nibao is a unique thrust fault-controlled and strata-bound disseminated gold deposit in southwestern Guizhou Province, China. In Nibao, pyrite is the major sulfide mineral and Au is structurally bound (Au^{+}) within the pyrite lattice. In this study, we conducted detailed analyses of the pyrite chemistry and S isotope composition in Nibao using laser ablation inductively coupled plasma mass spectrometry (LA-ICP-MS) and laser ablation multi-collector inductively coupled plasma mass spectrometry (LA-MC-ICP-MS), respectively. Through petrographic and pyrite chemical studies, four pyrite generations (Py1–Py4) were distinguished: framboidal pyrite (Py1, pre-ore sedimentary stage), clean pyrite overgrowing framboidal pyrite (Py2, pre-ore diagenetic stage), "spongy" pyrite (Py3, early ore stage), and overgrowth of narrow pyrite rims surrounding Py2/Py3 and disseminated pyrite associated with arsenopyrite (Py4, main ore stage). Among these, Py2 and Py4 are the most abundant.

The trace element content in Py2 is characterized by a wide range of As, Cu, Sb, and Pb concentrations (~2480–58100 ppm, ~55.4–1610 ppm, ~29.1–232 ppm, and ~24.1–376 ppm, respectively), while Py4 has the highest Au, As, Cu, and Se contents (~70 ppm, ~4200, ~1630 ppm, and ~38.3 ppm, respectively). The $\delta^{34}S$ values of pre-ore pyrites measured by LA-MC-ICP-MS in this study and the available data in the literature range broadly from −53.3 to 114.8‰, indicating that they were most likely generated by bacterial reduction from marine sulfate during sedimentation/diagenesis. Meanwhile, the $\delta^{34}S$ values of ore pyrites have relative narrow $\delta^{34}S$ values, mostly varying from −5 to 5‰, and indicating that the S was derived either from the average of sedimentary rocks or from a magmatic source.

Since igneous rocks are scarce in the region and the exposed (~77–99 Ma) are clearly younger than the mineralization age of the Nibao gold deposit (~141 Ma), a magmatic source is unlikely in Nibao. All pyrites in this study show a positive correlation (R^2 = 0.71) between Co and Ni, and the Co/Ni and Zn/Ni ratios of main stage Py4 are close to or within the range defined for a sedimentary–diagenetic origin, suggesting a sedimentary source is more likely in Nibao.

1. Introduction

Disseminated gold deposits (also known as Carlin-type gold deposits) are an important end member of low-temperature (~150–250 °C) epigenetic deposits that contribute significantly to the global supply of gold (~8%; Frimmel, 2008; Hu et al., 2017). These types of gold deposits are mainly located in Nevada, USA and southwestern China (Li and Peters, 1999; Gao et al., 2002; Hu et al., 2002, 2017; Cline et al., 2005; Su et al., 2008, 2012; Xia et al., 2009; Chen et al., 2011). The deposits in both regions formed in similar tectonic settings, with deposition of passive-margin sequences along a rifted cratonic margin with subsequent deformation (Cline and Hofstra, 2000; Hu et al., 2002; Muntean et al., 2011; Xie et al., 2018a). In both regions, typical ore-related alteration includes decarbonatization,

* Corresponding author at: State Key Laboratory of Ore Deposit Geochemistry, Institute of Geochemistry, Chinese Academy of Sciences, 99 Lincheng West Road, Guanshanhu District, Guiyang 550081, China.
E-mail address: xiayong@vip.gyig.ac.cn (Y. Xia).

https://doi.org/10.1016/j.oregeorev.2020.103446
Received 2 May 2019; Received in revised form 23 December 2019; Accepted 3 March 2020
Available online 06 March 2020
0169-1368/

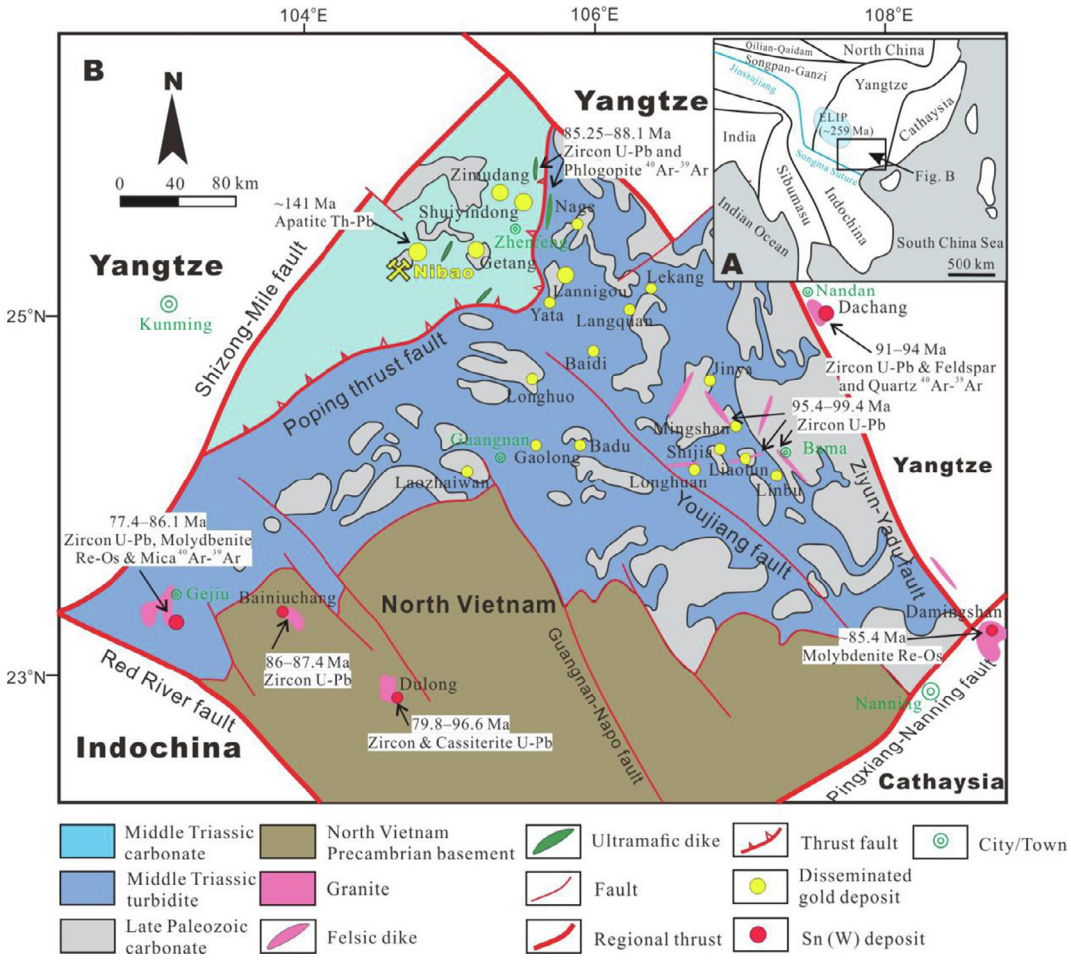

Fig. 1. (A) Regional tectonic framework of the Youjiang Basin; (B) Geology of the Youjiang Basin showing the distribution of disseminated gold deposits, igneous rocks and Sn-(W) deposits around the basin (modified from Cai and Zhang (2009) and Zhu et al. (2017)). Ages of the Sn-(W) deposits are summarized from Wang et al. (2004), Li et al. (2008), Cheng and Mao (2010), Cheng et al. (2013), Mao et al. (2013), and Xu et al. (2015). The ages of the ultramafic and felsic dikes are summarized from Liu et al. (2010) and Zhu et al. (2017), respectively. The age of the Nibao deposit is cited from Chen et al. (2019).

silicification, sulfidation, and argillization. Gold is invisible and ionically bound within arsenian pyrite lattices, and elements significantly correlated with Au include As, Sb, Hg, Tl, and Cu (Hu et al., 2002; Cline et al., 2005, 2013; Tan et al., 2015). One of the differences between the deposits in these two regions is the pH value of the ore-forming fluids – those in southwestern China are weakly acidic, while in Nevada they are more strongly acidic (Xie et al., 2018a).

The southwestern Guizhou (SW Guizhou) Province is the most abundant gold producing area of southwestern China. Following the discovery of the first disseminated gold deposit—the Banqi deposit—in 1978, more than 20 gold deposits and numerous occurrences have been discovered in SW Guizhou Province (Tu, 1992; Hu et al., 2002), including Shuiyindong (Xia, 2005; Tan et al., 2019), Jinfeng (Lannigou) (Zhang et al., 2003), Nibao (Wei et al., 2016), Zimudang (Liu et al., 2015), Getang (Hu et al., 2018), etc. Although these gold deposits have been mined for decades and their geological characteristics have been well documented (Xia, 2005; Xia et al., 2009; Liu et al., 2006; Wang et al., 2013; Hou et al., 2016), uncertainties remain regarding their origins due to conflicting data (e.g., the interpretation of S–H–O–C isotopic compositions), which hamper the development of a comprehensive genetic model. To date, at least three different models have been proposed for the origin of Au and the mineralizing fluids: (1) the sedimentary model suggests that Au was sourced from strata with pre-enriched sediments by the circulation of meteoric water (Zhang et al., 2003; Gu et al., 2012; Peng et al., 2014; Hu et al., 2017); (2) the metamorphic model argues for a metamorphic origin for mineralizing fluids related to crustal thickening and prograde metamorphism (Su et al., 2009, 2018); and (3) the magmatic model which proposes that Au and the related fluids were derived from concealed granitic intrusions (Liu et al., 2006; Zhang et al., 2010; Hu et al., 2018; Xie et al., 2018b).

Pyrite (FeS_2) is a common sulfide in disseminated gold deposits and it is an excellent recorder of the conditions under which it formed (Large et al., 2007, 2009, 2011; Franchini et al., 2015; Meffre et al., 2015; Gregory et al., 2016). However, it can form via sedimentary, metamorphic, and hydrothermal processes making interpretation of pyrite chemistry critical to understanding its origin. In disseminated gold deposits, Au-bearing pyrite is commonly fine-grained and texturally complex (Su et al., 2008, 2012; Large et al., 2009; Chen et al., 2015; Hu et al., 2018). It is difficult to convincingly determine the chemistry of ore-stage pyrite using traditional analyses of bulk ore samples or pyrite separates. The lack of definite trace element contents and isotopic compositions of different pyrite stages (i.e., pre-ore stage, ore stage, and post-ore stage) limits our understanding of the genesis of disseminated gold deposits. Recently, new in situ analytical methods, including laser ablation inductively coupled plasma mass spectrometry (LA-ICP-MS), for measuring trace element compositions, and laser ablation multi-collector inductively coupled plasma mass spectrometry (LA-MC-ICP-MS), for measuring S isotope compositions, have made it feasible to discriminate the chemistry of different generations of pyrite (Large et al., 2007; Gregory et al., 2016; Hou et al., 2016; Steadman and Large, 2016; Xie et al., 2018b; Hu et al., 2018).

The Nibao gold deposit contains a measured plus indicated resource

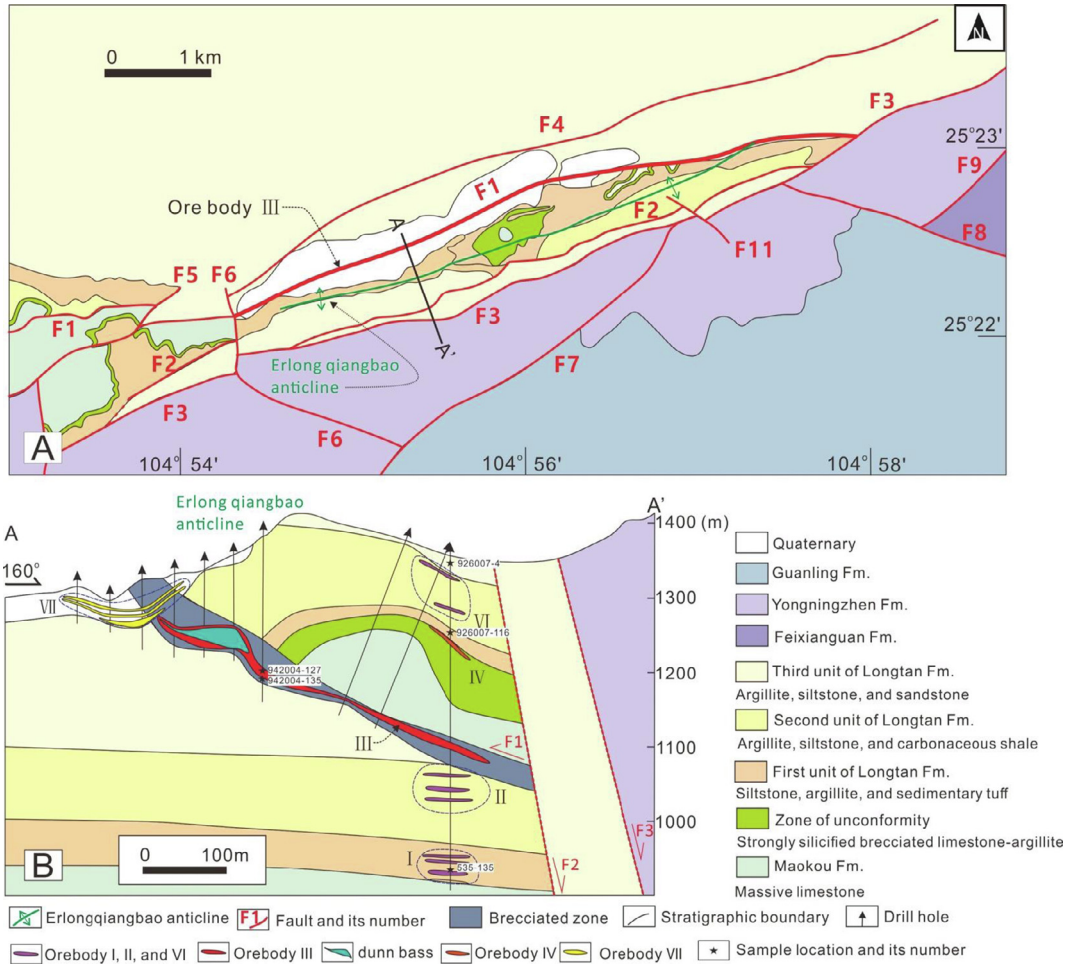

Fig. 2. (A) Simplified geologic plan map of the Nibao gold deposit. (B) A representative geological cross section (A–A′) of the Nibao gold deposit showing its major structures and stratigraphic units (Qi et al., 2014; Zheng et al., 2016). The location of this section is shown in Fig. 2A. The locations of five representative samples are also shown.

of over 60 t at 2.74 g/t Au and it is the third largest gold deposit in the region (Qi et al., 2014; Jin, 2017; Li et al., 2019). Recently, a large number of hypogene orebodies (100–500 m beneath the ground surface) were discovered in Nibao (Qi et al., 2014), and core samples from the most recent drilling program have provided an excellent opportunity to study this deposit.

Four generations of pyrite have been distinguished in Nibao based on petrographic studies: sedimentary framboidal pyrite preserved in the silicified rocks (Py1), relatively homogenous pyrite overgrown on Py1 hosted in the argillaceous rocks (Py2), spongy and porous pyrite overgrown on Py2 within the calcareous and argillaceous rocks (Py3), and overgrowth of pyrite rims surrounding Py2/Py3 and disseminated pyrite associated with arsenopyrite (Py4). Here we present LA-ICP-MS analyses for these four pyrite types and LA-MC-ICP-MS analyses for Py2 and Py4 from the Nibao gold deposit. The results help to differentiate between the generations of pyrite, clarify their genetic relationships to one another, and to assess the potential sources of Au and other elements in the Nibao deposit.

2. Regional geology

The SW Guizhou Province is within the Youjiang Basin along the southwestern margin of the Yangtze Craton (Peters et al., 2007; Cai and Zhang, 2009; Su et al., 2009; Yang et al., 2012; Tan et al., 2015; Su et al., 2018; Fig. 1A). The Yangtze Craton is an important part of the South China Block and hosts several successions of black shales, including the Neoproterozoic Duoshantuo Formation and the Cambrian Niutitang Formation. The thickness of black shale in the Duoshantuo Formation is ~60–70 m (Sahoo et al., 2016; Gregory et al., 2017), while that in the Niutitang Formation is thinner (~20 m, Zhang et al., 2016). The black shales in both formations contain abundant sedimentary pyrite. Sedimentary pyrite from Duoshantuo Formation contains up to ~1860 ppm of As, ~148 ppm of Sb, ~0.211 ppm of Au, and ~261 ppm of Ag (analyzed by LA-ICP-MS, Gregory et al., 2017). The average content of As, Sb, Au and Ag in sedimentary pyrites from Cambrian Niutitang Formation is 410 ppm, 250 ppm, 250 ppm, and 40 ppm, respectively (analyzed by EMPA, Zhang et al., 2016).

The Youjiang Basin is separated from the Yangtze Craton by the Shizong–Mile and Ziyun–Yadu faults to the northwest and northeast, respectively. It is separated from the Indochina Block to the southwest by the Red River Fault, and from the Cathaysia Block to the southeast by the Pingxiang–Nanning Fault. The southern edge of the Youjiang Basin is dominated by the North Vietnam terrane with a Precambrian basement (Fig. 1B).

Devonian-Triassic sedimentation is present throughout the Youjiang Basin, including platform, open continental shelf, shelf margin, slope and deep sea facies. The Early–Middle Devonian sequences, composed of sandstone, siltstone, and shale, unconformably overlie the southwestern margin of the Yangtze Craton. In turn, they are conformably overlain by a Late Paleozoic–Early Triassic succession with deep sea calcareous, siliceous, and volcanic rocks and pelites, which have been interpreted as a passive continental margin sequence (Zeng et al., 1995;

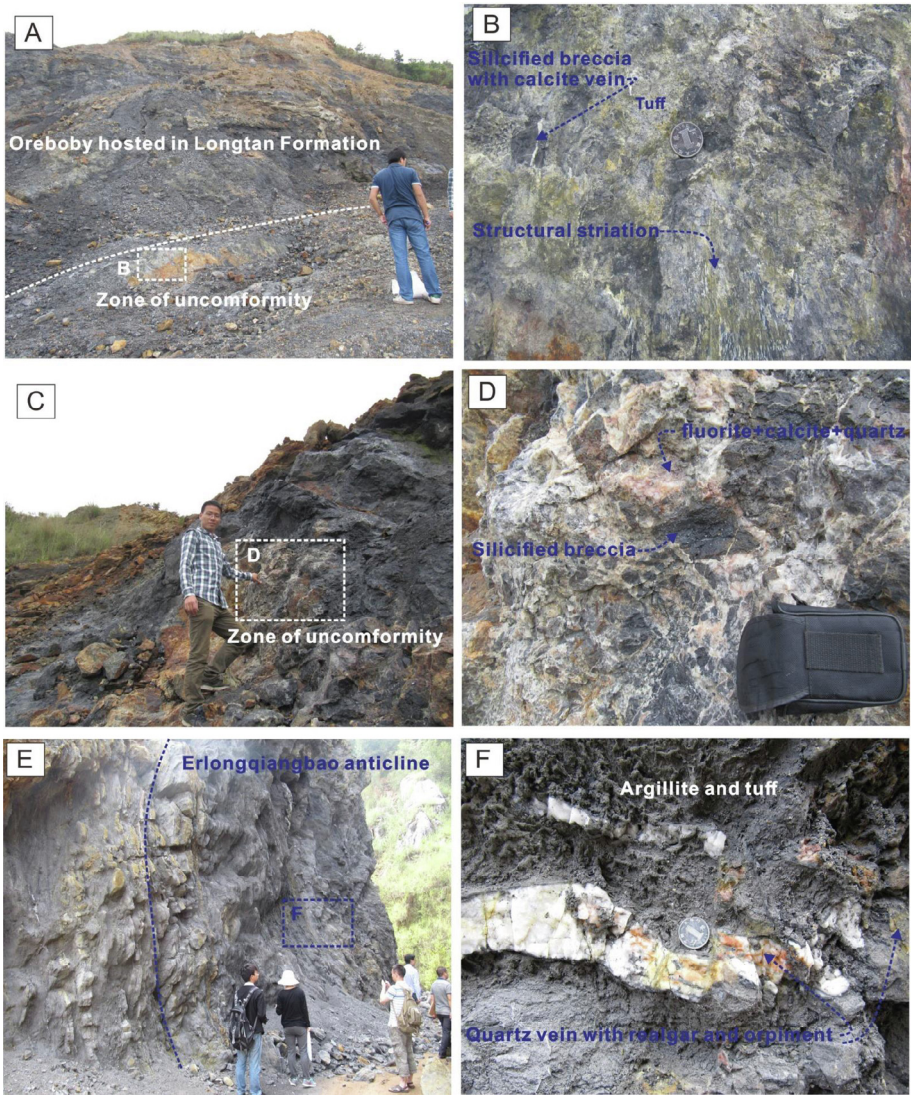

Fig. 3. Photographs showing typical geologic characteristics of the Nibao gold deposit. (A) Primary orebody in the Longtan Formation overlying the zone of unconformity. (B) Structure striations preserved on the surface of the unconformity. (C) Strongly silicified limestone in the zone of unconformity. (D) Silicified breccia cemented by fluorite, calcite, and quartz veinlets. (E) Location of the hinge zone of the Erlongqiangbao anticline. (F) Quartz vein with realgar and orpiment in argillite and tuff.

Qin et al., 1996; Chen et al., 2019). Additionally, this period also contains locally distributed shallow marine platform carbonates (Fig. 1B). The Middle Triassic strata can be divided into two sedimentary domains by the Poping thrust fault. Northwest of the thrust is a Late Paleozoic and Triassic carbonate platform, and a Triassic terrigenous clastic succession is present to the southeast (Fig. 1B).

Known igneous rocks are scarce in the region except for intrusive alkaline granites, and several felsic and ultramafic dikes (Fig. 1B). The ages of the granites, ultramafic dikes, and felsic dikes have been constrained by various methods, and range from ~77 to 96 Ma (Wang et al., 2004; Li et al., 2008; Cheng and Mao, 2010; Cheng et al., 2013; Xu et al., 2015), ~88 to 85 Ma (Liu et al., 2010), and ~95 to 99 Ma (Zhu et al., 2017), respectively.

The orebodies of disseminated Au deposits in SW Guizhou are primarily hosted within Late Paleozoic to Triassic strata (Fig. 1B). Typically, they are also controlled by structures, including: short-axis anticlines (domes) (e.g., the Shuiyindong gold deposit; Su et al., 2012), high-angle faults (e.g., the Lannigou gold deposit; Chen et al., 2011), thrust faults (e.g., the Nibao gold deposit; Qi et al., 2014), and paleokarst planes or zones of unconformity (e.g., the Getang gold deposit; Hu et al., 2018).

3. Deposit geology

The Nibao gold deposit is situated along the northwestern margin of the Youjiang Basin (Fig. 1B). The stratigraphic sequence in Nibao primarily includes the Middle Permian Maokou, the Upper Permian Longtan, the Lower Triassic Feixianguang and Yongningzhen, and the Middle Triassic Guanling Formations (Fig. 2). The Middle Permian Maokou Formation is dominated by > 100 m thickly bedded massive limestone. The Upper Permian Longtan Formation can be further divided into three stratigraphic units in the Nibao deposit. The lowest unit consists of carbonaceous and calcareous siltstone, argillite, and gray–dark gray sedimentary tuff (Fig. 3A). The tuff is variable in thickness (~0–30 m) and its chemical composition is consistent with that of the Emeishan basalts (Qi et al., 2014; Hu et al., 2018). The second unit is composed of argillite, siltstone, and carbonaceous shale. The third unit is composed of silicified limestone, carbonaceous argillite, siltstone, and sandstone (Qi et al., 2014; Jin, 2017; Li et al., 2019). Both the lowest and second units of the Longtan Formation are the main strata that host part of the primary ore. A zone of unconformity that exists between the Longtan Formation and Maokou Formation in Nibao is characterized by strongly hydrothermally silicified and brecciated

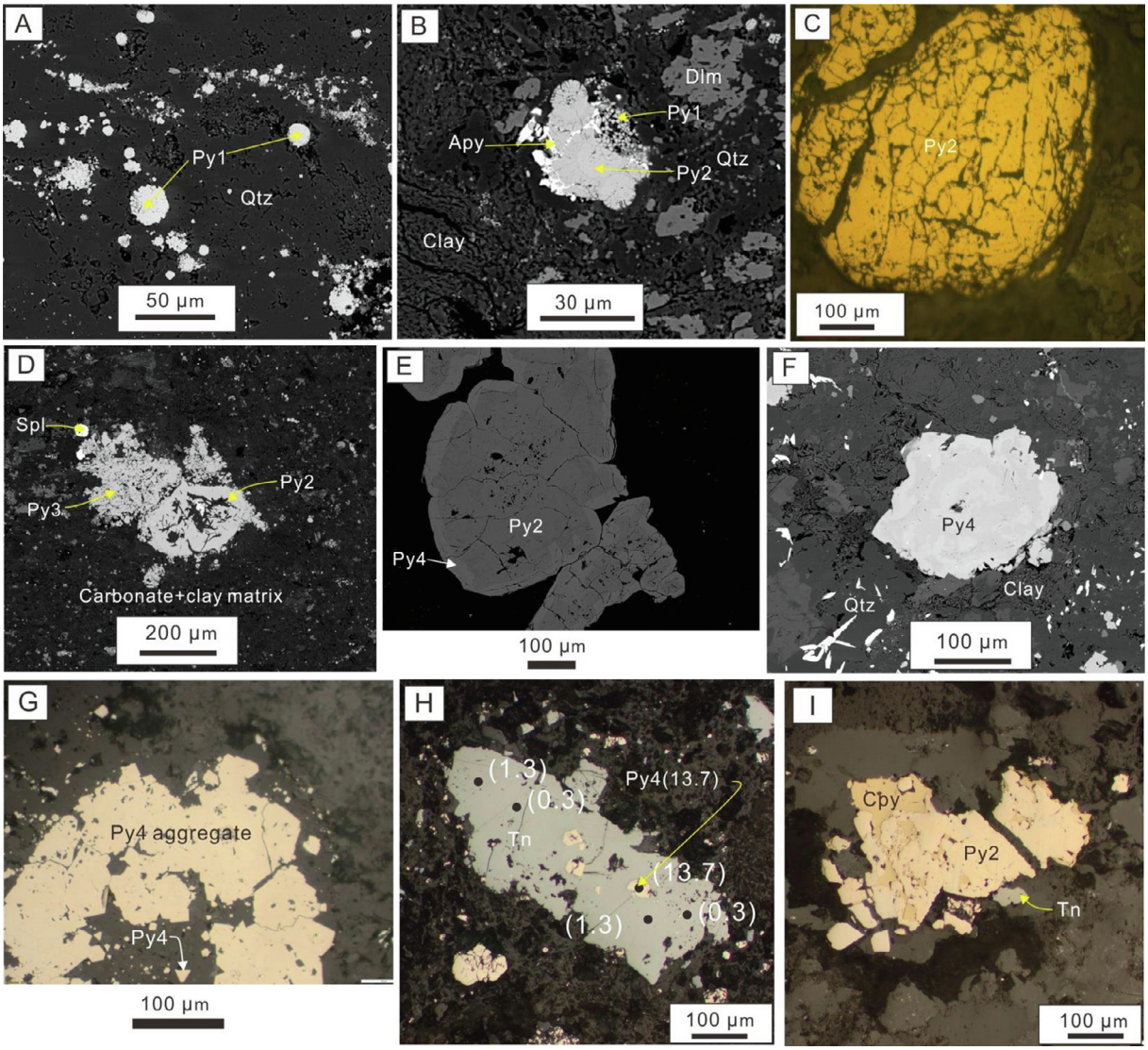

Fig. 4. Morphological and textural features of different generations of pyrite in the Nibao gold deposit. (A) Framboidal Py1 surrounded by Qtz (BSE image). (B) Framboidal Py1 overgrown by Py2, and Apy1 filling the fracture (BSE image). (C) Coarse Py2 grains with many micro-fractures (RPPL image). (D) Smooth subhedral Py2 and spongy porous Py3 hosted in a carbonate matrix (BSE image). (E) Py2 overgrown by a rim (20–40 μm) of Py4 (BSE image). (F) Individual Py4 grain associated with Apy, Cal, Qtz, and clay (BSE image). (G) Py4 aggregate and disseminated fine-grained Py4 (RPPL image). (H) Individual Py4 grains surrounded by tennantite (RPPL image). The black spot represents the laser spot and its gold content (ppm) is shown in brackets. (I) Smooth Py2 partly replaced by Cpy (RPPL image). *Abbreviations:* Apy, arsenopyrite; Cal, calcite; Cpy, chalcopyrite; Py, pyrite; Qtz, quartz; Spl, sphalerite; Tn, tennantite. BSE, backscattered electron; RPPL, reflected plane polarized light.

limestone–argillite (Fig. 3A–D), and it hosts lower grade orebodies (Fig. 2). The Lower Triassic Feixianguan Formation is mainly composed of siltstone and mudstone, while the Lower Triassic Yongningzhen Formation is composed of bedded dolostone, limestone, and marl. The Upper Triassic Guanling Formation consists of thickly bedded dolostone and limestone.

The dominant structures in the Nibao deposit include Erlongqiangbao anticline, F1 thrust fault, and several small fractures (Fig. 2). The Erlongqiangbao anticline was formed by the thrusting movement of F1 (Fig. 3E). The F1 thrust fault also caused a breccia zone (Fig. 2B). The volcanic tuff, argillite, siltstone, and limestone in the F1 breccia zone were brecciated by later tectonic and hydrothermal activity.

A newly published Th–Pb dating of hydrothermal apatite via secondary ion mass spectrometry (SIMS) has determined an age of 141 ± 3 Ma for the mineralization of the Nibao deposit (Chen et al., 2019). The orebodies in the deposit can be divided into four types (Fig. 2B): (1) oxidized orebodies (Orebody VII) hosted in Quaternary sediments; (2) hypogene orebodies (Orebodies I, II, and VI) in the Longtan Formation; (3) laminar orebodies (Orebody IV) hosted within the zone of unconformity; (4) giant orebodies (Orebody III) in the F1 breccia zone. Gold mineralization is primarily confined to the F1 breccia zone, the unconformity, and the Longtan Formation, and is hosted within silicified and brecciated limestone, argillite, and tuff.

The primary sulfide mineral in Nibao is pyrite, with minor arsenopyrite, and trace sphalerite, realgar, orpiment, tennantite, and chalcopyrite (Figs. 3F and 4). Other gangue minerals include fluorite, calcite, dolomite, ankerite, quartz, and clay minerals (e.g., illite, kaolinite) (Figs. 3D, F and 4). Sulfides in the pre-ore stage include the framboidal pyrite (Py1) and the relatively homogeneous overgrowing pyrite (Py2) in silicified limestone and argillite (Fig. 4A–C). The early ore stage is dominated by spongy pyrite (Py3) hosted in calcareous and argillic rocks (Fig. 4D). The main ore stage is characterized by a narrow pyrite rim (5–40 μm) and disseminated pyrite (Py4) associated with arsenopyrite in silicified carbonate breccias (Fig. 4E–G). Sulfides in the late ore stage are dominated by sphalerite, tennantite, chalcopyrite, realgar

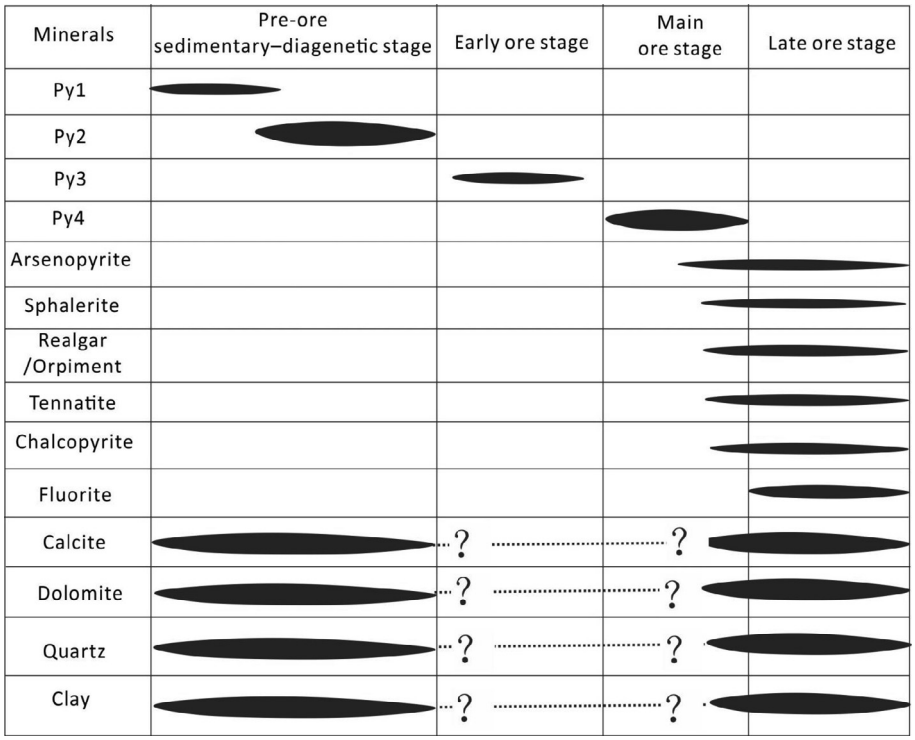

Fig. 5. Summary of the paragenetic sequence from the pre-ore stage to the late ore stage in the Nibao gold deposit.

Table 1
Locality information for samples used for laser ablation inductively coupled plasma mass spectrometry (LA-ICP-MS) and LA multicollector ICP-MS (LA-MC-ICP-MS) analyses in Nibao.

Sample No.	Location	Sulfide	Lithological description
926007-4	Distal to ore; the third unit of the Upper Permian Longtan Formation	Py	Grey-black strongly silicified limestone
926007-116	Distal to ore; the first unit of the Upper Permian Longtan Formation	Py, Aspy,	Off-white micrite with tuff
942004-127	Within orebody III; the F1 breccia zone	Py, Aspy	Off-white argillaceous dolomitic breccia, cemented by ferrodolomite
942004-162	Within Orebody III; the F1 breccia zone	Py	Grey-black silicified limestone across cut by calcite veins
535-135	Near or within Orebody I; the first unit of the Upper Permian Longtan Formation	Py, Aspy, Mcs	Grey-black argillaceous conglomerate
545-140	Near Orebody III; the F1 breccia zone	Py, Aspy	Grey-black argillaceous conglomerate

Abbreviations: Aspy, arsenopyrite; Mcs, marcasite; Py, pyrite.

Table 2
Summary of common textures, gold content, and interpreted timing for main pyrite types in Nibao.

Pyrite types	Texture	Gold content (ppm)	Interpretation of timing	Evidence for timing
Py1	Framboidal pyrite cluster	Invisible gold Range: 0.028–1.74 Median: 0.661	Sedimentary	Overgrown by all later py types
Py2	Homogenous euhedral to subhedral pyrite	Invisible gold Range:0.05–1.33 Median: 0.29	diagenetic	Intimately related to Py1, Commonly overprints and overgrows py1, and overgrown by pyrite rims (interpreted as Py3 or Py4)
Py3	Spongy and porous pyrite	Invisible gold Range: bdl-1.18 Median: 0.599	Early ore stage	Overgrowing py2 and overgrown by homogeneous pyrite rim (interpreted as Py4)
Py4	1. Outmost narrow rim 2. Euhedal to subhedral grain aggregate 3. disseminated grain	Invisible gold And/or micronuggets Range: 4.53–206 Median: 70	Intermediate ore stage	The outmost pyrite rim, overgrowing on all earlier py types

Abbreviations: bdl, below detection limit.

and orpiment (Figs. 3F and 4D, F, H, I). The mineral assemblage of each stage is summarized in Fig. 5.

Hydrothermal alteration in Nibao is pervasive and involves a combination of silicification, carbonatization, argillization, and sulfidation. Silicification is typically recognized as quartz veinlets (Fig. 3F). Carbonatization is the most common form of alteration and preferentially occurs as calcite veins in altered rocks (Fig. 3B). Argillic alteration, characterized by clay minerals such as illite and kaolinite, is mainly present in the argillite and sedimentary tuff (Figs. 3E, F and 4B, D–F).

Table 3
Summary of LA-ICP-MS analyses of pyrite types from the Nibao gold deposit, SW Guizhou Province, China (all elements in ppm).

Element	Py1 (n = 11)			Py2 (n = 12)			Py3 (n = 13)			Py4 (n = 30)		
	Min	Max	Median	Min	Max	Median	Min	Max	Median	Min	Max	Median
Mn	1.03	5680	981	0.716	1.26	1	81.7	1080	328	0.801	5.06	2.14
Co	12.3	155	49.6	2.17	2470	9.15	68.8	304	144	1.02	414	31.8
Ni	88.2	417	197	0.224	22,400	18.3	174	520	301	3.02	524	109
Cu	5.78	227	101	55.4	1610	854	52.4	188	112	815	4070	1630
Zn	0.429	155	26.7	7.57	496	16.2	2.59	6.3	3.81	0.443	3430	2.54
As	104	4630	3500	2480	58,100	37,700	6580	42,800	20,500	24,200	78,800	42,000
Se	4.39	37.8	19	16.3	42.9	24.7	1.48	8.82	2.81	21.1	59.5	38.3
Mo	1.08	44.5	7.52	bdl	5.84	0.056	bdl	5.44	0.061	bdl	13	0.158
Ag	bdl	2.3	0.395	0.386	2.59	0.959	0.226	2.85	0.662	0.295	7.53	3.1
Cd	bdl	6.98	0.68	0.08	1.12	0.123	0.072	3.28	0.643	bdl	23.1	1.1
Sn	0.2	4.46	1.43	0.666	15.8	1.55	0.328	1.31	0.502	0.117	10.5	0.271
Sb	0.67	222	40.4	29.1	232	101	120	402	228	21.1	458	128
Te	bdl	1.9	0.358	bdl	37.8	0.15	bdl	0.447	0.138	bdl	1.81	0.65
W	bdl	5.05	2.3	bdl	7.99	0.368	0.097	18.5	2.79	0.032	18.5	0.975
Au	0.028	1.74	0.661	0.05	1.33	0.29	bdl	1.18	0.599	4.53	206	70
Tl	0.113	24.2	5.25	0.352	13.9	6.24	2.49	19	5.6	2.66	39.9	10.5
Pb	0.312	22.4	6.46	24.1	376	54.7	6.23	13.2	9.95	6.44	73.5	25.8
Bi	0.008	0.556	0.085	0.106	6.48	0.475	0.043	0.979	0.15	0.076	1.57	0.375
Th	bdl	1.26	0.395	0.014	6.5	1.5	0.387	16.4	1.52	bdl	12.6	0.41
U	bdl	5.36	0.669	0.035	5.65	0.806	0.068	1.19	0.187	bdl	28.9	0.411

Abbreviations: bdl, =below detection limit.

4. Samples and analytical methods

4.1. Sample preparation

More than 50 samples from outcrops and drill holes with different Au grades were collected and 30 samples were made into polished laser mounts. The laser mounts were prepared by impregnating samples in epoxy resin and polishing to 1 μm using diamond polishing compounds. Reflected light microscopy and scanning electron microscopy (SEM) were conducted on all samples to determine the mineral assemblages, textures, and cross-cutting relationships. After optical petrography and SEM examinations, five representative samples were chosen for analyzing the trace element content of pyrite using LA-ICP-MS. One laser mount was selected for the in situ S isotope analysis of pyrites using LA-MC-ICP-MS. The information for the samples analyzed by LA-ICP-MS and LA-MC-ICP-MS is summarized in Table 1.

4.2. LA-ICP-MS spot analysis

Concentrations of trace elements in pyrite were measured by the LA-ICP-MS at the Centre for Ore Deposit and Earth Sciences (CODES), University of Tasmania (UT). The instrument consisted of a Coherent 193 nm ArF gas-charged excimer laser (Coherent Inc., USA) coupled with an Agilent 7700 quadrupole ICP-MS (Agilent Tech., USA). The laser methodology employed at CODES for trace element analysis was described in detail by Large et al. (2009) and Danyushevsky et al. (2011) and is briefly summarized in here. The UT in-house STDGL2b2 standard glass which contains 43 elements, 40 of which are quantifiable or semi-quantifiable, was utilized as a standard reference (Danyushevsky et al., 2011; Steadman et al., 2015), as well as the United States Geological Survey (USGS) basalt glass GSD-1G (Guillong et al., 2005) and an in-house pyrite (Gilbert et al., 2014a,b). Beam sizes utilized in the analyses were based on the size variations in sulfides and ranged from 19 to 39 μm. First, the spot was pre-ablated with five pulses to eliminate the effect of surface contamination. The background was measured for 30 s prior to an 11–60 s period of laser ablation for each analysis. The analyses were conducted in an atmosphere of pure He, which was introduced at a rate of 0.71 L/min. To improve aerosol transport, the He gas was mixed with Ar (1.231 L/min) after exiting the cell and then passed through a pulse-homogenizing device before hitting the torch inside the ICP-MS (Danyushevsky et al., 2011; Steadman et al., 2015).

4.3. LA-ICP-MS image analysis

Laser images were obtained under similar conditions as spot analyses except that a smaller beam diameter (10 or 15 μm) and a 10 Hz pulse rate were used. A series of parallel lines were ablated at a speed of 10 μm/s instead of individual spot analysis. The data obtained from parallel ablation lines were then used to create a trace element image, as described in detail by Steadman et al. (2013).

4.4. LA-MC-ICP-MS analysis

The $^{34}S/^{32}S$ isotope ratios of pyrites were measured by the LA-MC-ICP-MS at the USGS in Denver, Colorado. Analyses were performed using a Teledyne CETAC Photon Machines G2 Excimer laser ablation (LA) system (Teledyne Technologies, Inc., USA) coupled to a Nu Instruments HR® MC-ICP-MS (Nu Instruments, Ltd., UK). A 20 μm spot size was used for analyzing pyrite and reference material samples. Operating procedures were conducted under the conditions described in detail by Pribil et al. (2015) and Xie et al. (2018b).

5. Results

5.1. Occurrence, texture, and LA-ICP-MS spot analyses of pyrite

Pyrite is the most abundant sulfide mineral in the Nibao gold deposit and displays great textural variety. Four main types of pyrite have been recognized based on morphology, texture, and geochemistry (Table 2). The 66 LA-ICP-MS spot analyses performed in this study sampled all four of the pyrite types identified in the Nibao gold deposit. Table 3 and Figs. 6 and 7 summarize the results of the pyrite analyses that include measurements of Py1 (n = 11), Py2 (n = 12), Py3 (n = 13), and Py4 (n = 30). The complete LA-ICP-MS spot analysis dataset, including errors, detection limits, and precision estimates for each spot, is listed in Supplementary Table S1.

5.1.1. Py1

The pre-ore sedimentary pyrite, Py1, is best developed in the silicified limestone, argillite, and black shale of the Longtan Formation. It generally consists of very fine (1–3 μm) grains and framboidal pyrite clusters (> 10 μm) or fine-grained pyrite aggregates surrounded by quartz and/or clay (Fig. 4A, B). Since Py1 was too fine-grained for LA-ICP-MS analysis, a laser diameter of 19 μm was applied to its

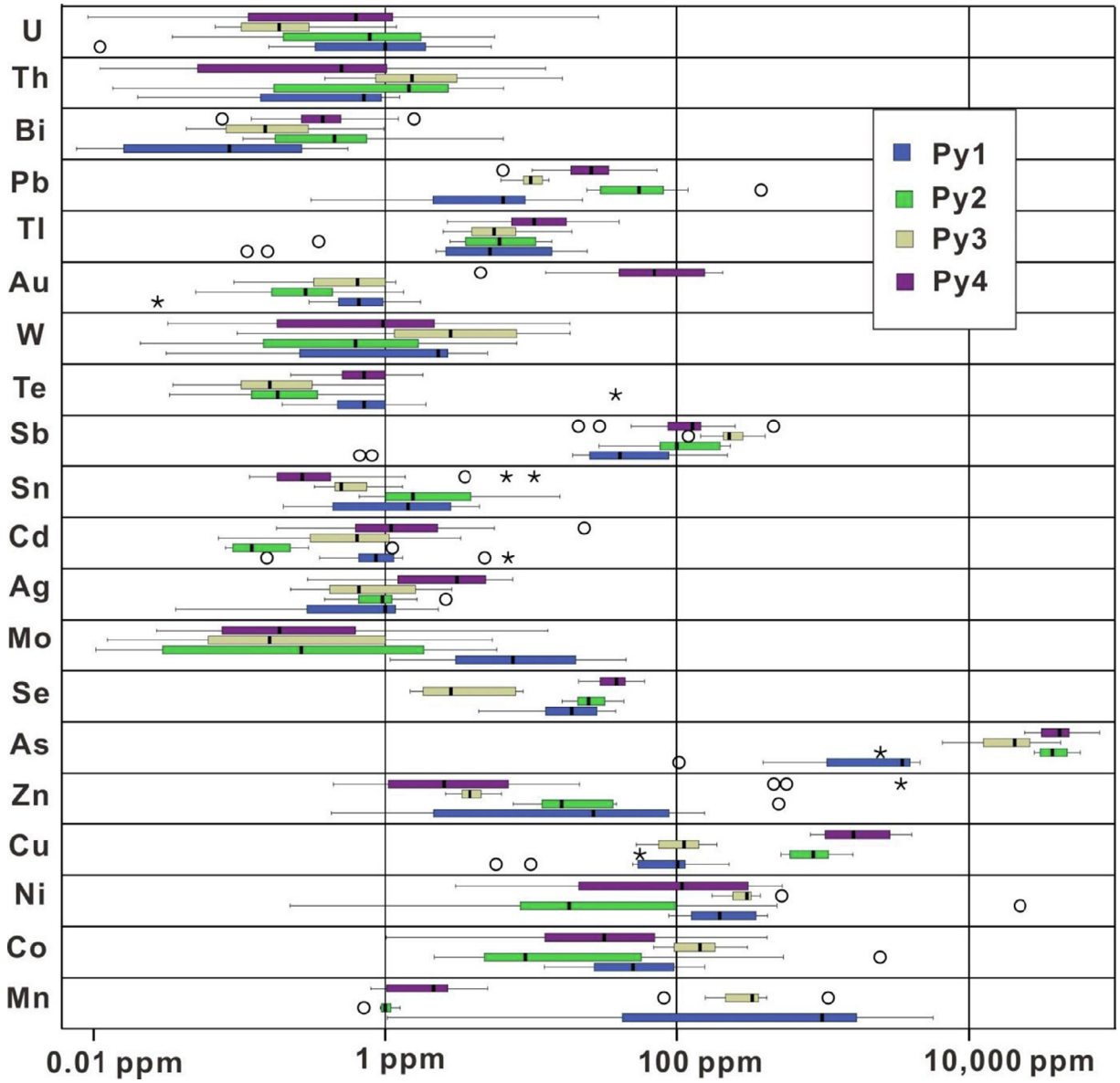

Fig. 6. Box plot of trace element contents of the four pyrite types (Py1–Py4).

aggregates, which contain ~90 vol% of Py1. Gold in Py1 aggregates is detectable and varies from 0.028 to 1.74 ppm (median = 0.661 ppm). Aggregates of Py1 contain a wide range of trace elements, including Mn (1.03–5680 ppm), As (104–4630 ppm), Co (12.3–155 ppm), Ni (88.2–417 ppm), Cu (5.78–227 ppm), Mo (1.08–44.5 ppm), and Sb (0.67–222 ppm) (Fig. 6; Table 3).

5.1.2. Py2

The pre-ore diagenetic pyrite (Py2) is commonly formed as subhedral grains (~50 μm) that overgrow framboidal Py1 in argillite (Fig. 4B). Separate coarse subhedral Py2 grains occur in argillite, limestone, black shale, and pyroclastic rocks. The size of this pyrite type can be very large (up to 500 μm), and Py2 is commonly characterized by many microfractures (Fig. 4C). In a pyrite composite (Fig. 4D, E), Py2 is usually overgrown by later spongy pyrite and/or later narrow, clean pyrite rims in argillite and carbonaceous rocks near or within the orebody. Commonly, the surface of most Py2 is clean and homogeneous rather than porous, as in framboidal pyrite and the later pyrite generations. Gold content in Py2 ranges from 0.05 to 1.33 ppm, with a median of 0.29 ppm. Additionally, Py2 displays a wide range of Cu (55.4–1,610 ppm), As (2480–58100 ppm), Sb (29.1–232 ppm), and Pb (24.1–376 ppm) contents, and low contents of Mn (0.716–1.26 ppm) and Mo (from below the detection limit to 5.84 ppm) (Fig. 6; Table 3).

5.1.3. Py3

The early ore stage (Py3) is spongy and porous (~50 μm), occurring in or near the orebody (mainly Orebody I) (Fig. 4D). Because of its spongy and porous texture, the chemistry of Py3 can include a mix of ~5–10% of the matrix composition. The median Au content of Py3 is 0.599 ppm, ranging from the below detection limit to 1.18 ppm. Additionally, Py3 has higher contents of Mn (81.7–1080 ppm), Co (66.8–304 ppm), and Ni (174–520 ppm) than that of Py2, but the contents of Cu (52.4–188 ppm), As (6578–42,800 ppm), Zn (2.59–6.3 ppm), Se (1.48–8.82 ppm) and Pb (6.23–13.2 ppm) are lower (Fig. 6; Table 3).

5.1.4. Py4

The main ore stage pyrite (Py4) generally forms a narrow, clean inclusion-poor rim (5–40 μm) upon earlier pyrite generations (Fig. 4E). It also occurs as a median, euhedral, disseminated grain (~100 μm) hosted in the silicified carbonate breccia within Orebody III (Fig. 4F). Individual Py4 grains can be assembled to form a pyrite aggregate

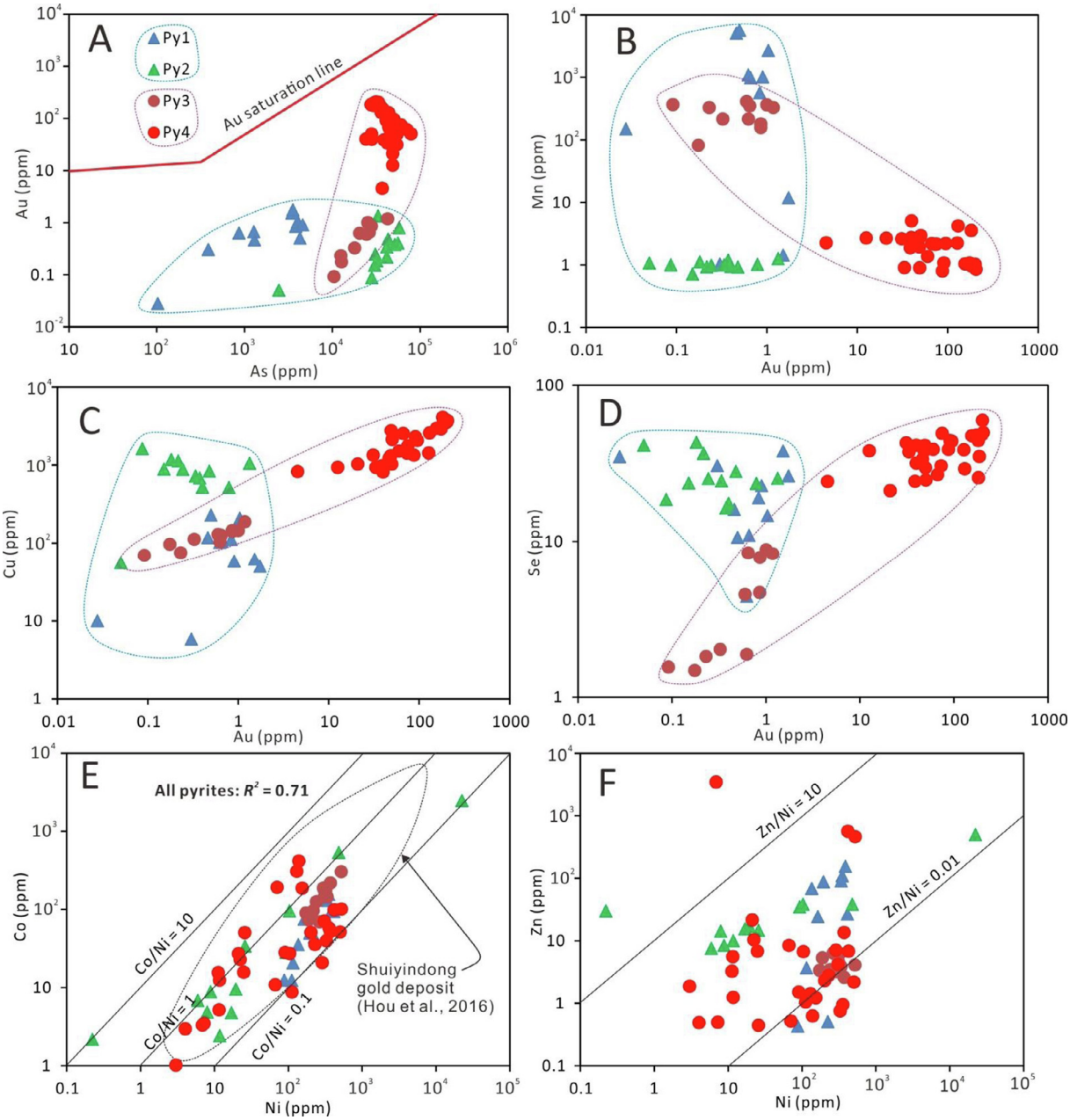

Fig. 7. Trace element contents and correlations for different types of pyrite from the Nibao gold deposit. The blue dashed line groups Py1 and Py2, and the purple dashed line groups Py3 and Py4. (A) Au vs. As; (B) Mn vs. Au; (C) Cu vs. Au; (D) Se vs. Au; (E) Co vs. Ni; (F) Zn vs. Ni. (For interpretation of the references to colour in this figure legend, the reader is referred to the web version of this article.)

(Fig. 4G). Additionally, Py4 has high contents of Au (4.53–206 ppm), As (24,200–78,800 ppm), Cu (815–4070 ppm), and Se (21.1–59.5 ppm), but low contents of Mn (0.801–5.06 ppm) (Fig. 6; Table 3).

5.2. LA-ICP-MS trace element maps of pyrite

In addition to spot analyses, trace elements in two pyrite samples from the Nibao deposit were imaged in detail using LA-ICP-MS. Fig. 9 shows a laser ablation trace element map of sample 535–135 from the relatively small footwall orebodies (Orebody I; Fig. 2B). This pyrite composite is composed of at least three pyrite-matrix or pyrite-only zones. The core of the pyrite composite (Py2) is oblong and inclusion-poor, with very few trace elements. The main zone (Py3) is more porous and the matrix may make up 1–5% of the total. Compared with the core, the main zone has relatively high trace element concentrations, including Co (100–500 ppm), Ni (100–500 ppm), Cu (10–100 ppm), As (1000–10,000 ppm), Sb (100–1000 ppm), Tl (1–10 ppm), and Pb (1–10 ppm), consistent with the spot analysis results. The outmost rim (Py4) is narrower (5–20 μm), cleaner, and less porous than the main zone. Most trace elements are concentrated in the outmost rim: Co (100–500 ppm), Ni (100–500 ppm), Cu (100–500 ppm), As (10,000–50,000 ppm), Ag (1–10 ppm), Sb (100–500 ppm), Au (10–50 ppm), Tl (1–50 ppm), and Pb (10–50 ppm). These trace elements have greater concentrations than the main zone except for Pb, which is mostly concentrated in the main zone. The zonation of Au is much narrower than those of Co, Ni, As, Sb, and Tl.

The second laser ablation trace element map of sample 926007-116 (Fig. 10) shows no apparent zonation in the pyrite composite under reflected light. However, at least two zones were observed with abundant trace elements. The core of the pyrite composite (Py2) is especially

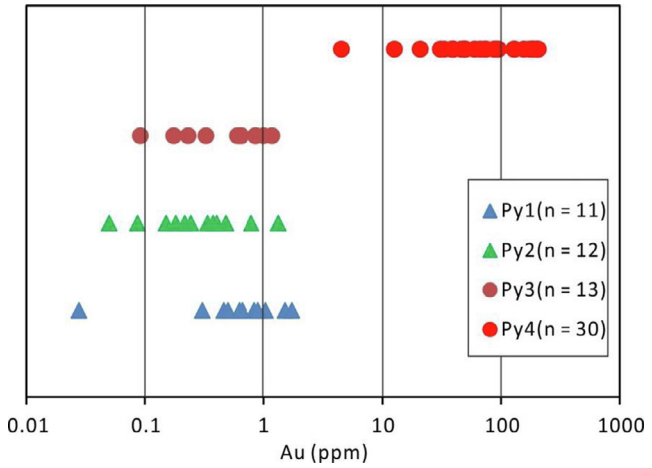

Fig. 8. Au contents (ppm) in different types of pyrites in the Nibao gold deposit.

depleted in Co, Ni, and Au, but concentrated in Cu (100–1000 ppm), Sb (500–1000 ppm), and Tl (1–10 ppm). The outer zone (Py4) is relatively enriched in Co (500–1000 ppm), Ni (500–1000 ppm), and Au (1–50 ppm). Arsenic is concentrated in this pyrite, but no clear zonation was observed.

5.3. LA-MC-ICP-MS sulfur isotopes of pyrite

In situ $\delta^{34}S$ values of Py2 and Py4 were quantified by LA-MC-ICP-MS analyses. The $\delta^{34}S$ data for Py1 and Py3 could not be obtained in this study because they are too rare in the analyzed sample. The $\delta^{34}S$ values of Py2 this study and the available in situ S isotope data of the pre-ore pyrite in the literature range broadly from −53.3 to 114.8‰, while the $\delta^{34}S$ values of Py4 in this study and that of ore-pyrite from the literature have relative narrow $\delta^{34}S$ values, mostly varying from −5 to 5‰ (Jin, 2017; Zheng, 2017; Li et al., 2019; Table 4; Fig. 11). A compilation of in situ S isotope dataset of the Nibao deposit is listed in Supplementary Table S2.

6. Discussion

6.1. Nature of pyrite (Py1–Py4)

Although framboidal pyrite (Py1) may be formed during metamorphism and hydrothermal alteration (Scott et al., 2009), it is commonly formed in a sedimentary environment (Love, 1971; Wilkin and Barnes, 1997). Framboidal pyrite in the Nibao gold deposit is restricted to the silicified limestone, argillite, and black shale of the Longtan Formation, rather than occurring in hydrothermal veins. Therefore, Py1 likely formed during sedimentation prior to the onset of hydrothermal processes. According to the results of LA-ICP-MS spot analyses, framboidal pyrite is relatively enriched in Mn but deficient in As when compared to hydrothermal pyrite (Py3 and Py4), and is similar to the composition of sedimentary–diagenetic pyrites that developed in other sediment-hosted gold deposits (Large et al., 2007, 2009; Wang and Zhu, 2015; Hou et al., 2016; Li et al., 2019).

The pre-ore diagenetic pyrite (Py2) precipitated on Py1 and most individual Py2 has been observed distally to the orebody, suggesting that Py2 likely formed during the diagenetic stage. The microfractures on Py2 indicate that Py2 was affected by later tectonic activity, possibly the F1 thrust fault. Although Py2 has a relatively high Cu content, it is not positively correlated with the Au content, as in the hydrothermal pyrite (Py3 and Py4) (Fig. 7C). Relatively higher contents of trace elements in Py2 over Py1 may be a result of further diagenesis (Gregory et al., 2016). The decrease in the Mn and Mo content from Py1 to Py2 suggests that the late diagenetic environment was characterized by insufficient seawater recharge because Mn and Mo in pyrite are mostly supplied by the water column and would have been exhausted early during diagenesis (Gregory et al., 2014).

The early ore stage Py3 can only be observed within or near the orebody. It usually contains low Au content, overgrows Py2, and is overgrown by a narrow clean pyrite rim (Py4), suggesting that Py3 is most likely to be produced early during ore formation. The porous texture of Py3 is similar to the pyrite formed during early ore stage in other disseminated Au deposits, such as the Shuiyindong Au deposit (Hou et al., 2016). The high Mn content in Py3 suggests that Py3 may have developed in a relatively oxygenated solution (Maslennikov et al., 2009; Basori et al., 2018).

The overgrowing relationship with other pyrite types and the high Au content of Py4 suggest that Py4 formed during the main ore stage, while the decreased of Mn contents from Py3 to Py4 suggests that the hydrothermal fluids became reduced during ore formation (Maslennikov et al., 2009; Basori et al., 2018).

6.2. Gold distribution in pyrite

The results of the LA-ICP-MS analyses for Au from Py1 to Py4 are illustrated in Fig. 8. The detectable Au concentrations of the four pyrite generations varied from 0.028 to 206 ppm. The median Au progressively increased from 0.29 ppm in Py2, to 0.599 ppm in Py3, to 0.661 ppm in Py1, and to 70 ppm in Py4 (Table 3). Compared with the other pyrite generations, Py4 had a much higher Au content. Gold concentrations in Py1 and Py2 from the Nibao gold deposit were higher than that in common sedimentary–diagenetic pyrite (~0.16 ppm), as determined by Gregory et al. (2015a). However, the resolution of LA-ICP-MS is not sufficient to determine whether this is due to the strata being anomalously enriched in Au or if Au was adsorbed onto the surface of Py1 and Py2 during the subsequent hydrothermal activities (Hu et al., 2018).

Although micron to submicron particles of visible Au have been previously detected in the region (the Shuiyindong deposit, Su et al., 2008), no visible Au was observed during the optical microscopy or SEM imaging portions of this study, even for pyrites with maximum Au concentrations (i.e., 206 ppm in Py4). This suggests that Au is either structurally bound (e.g., Au^{+}) or occurs as nanoparticles of native Au (Au^{0}) in the pyrite lattice (Simon et al., 1999; Liu, 2003; Deditius et al., 2008; Hou et al., 2016; Hu et al., 2018; Li et al., 2019). However, according to the binary diagram of Au versus As (Fig. 7A), all pyrite spots were below the solubility line of invisible Au in pyrite, as determined by Reich et al. (2005), indicating that the ore-forming solutions were unsaturated with respect to native Au. Thus, it is more likely that Au is structurally bound (Au^{+}) in the pyrite lattice. This is also consistent with the relatively homogeneous distribution of Au in laser ablation images of representative Py4 (Figs. 9 and 10).

Similar to most Carlin-type gold deposits, many main ore stage pyrites from the Nibao deposit are enriched both in Au and As, as well as in other elements, including Cu and Sb. The Au contents were strongly enriched during the precipitation of Py4 (Figs. 7A and 8), and Py4 is also paragenetically related to other gangue minerals, including quartz, dolomite, calcite, and fluorite, suggesting that the evolution/reaction of the fluids was accompanied by the appearance of Au, As, and other trace elements (Hou et al., 2016). In the Au versus As binary diagram (Fig. 7A), the plots of Py3 and Py4 form an elongated and nearly vertical pattern located at the Au–As-rich end of the spectrum, implying that Au concentrations in the Nibao deposit are not correlated with As (Hou et al., 2016). This is also consistent with the results of laser ablation images (Figs. 9 and 10), in which the zonation of Au is much narrower than that of As.

6.3. Implications for the origin of Au

In Carlin-type ore systems, because ore fluids are enriched in

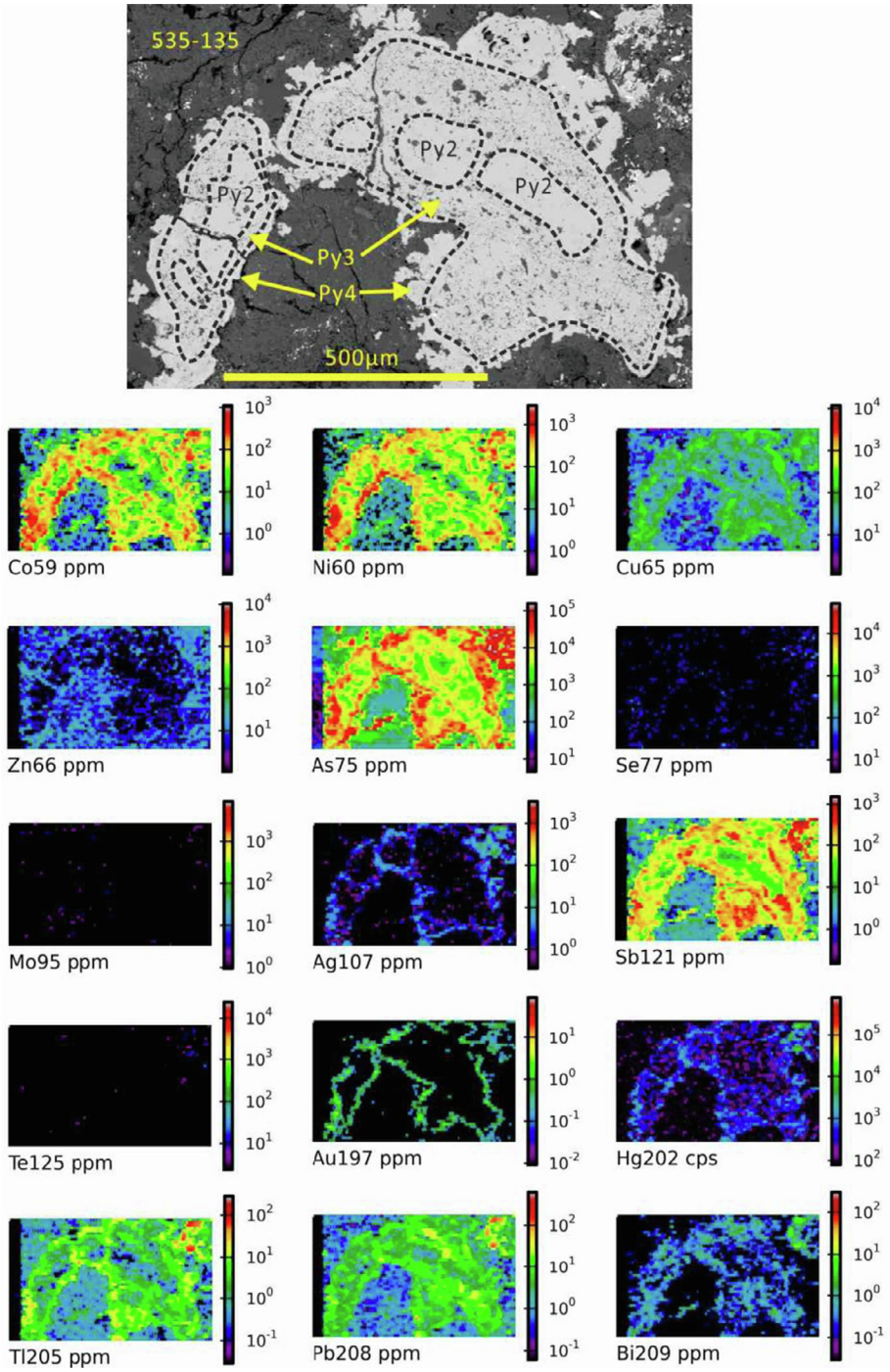

Fig. 9. Sample 535–135 LA-ICPMS trace element images. This pyrite composite is composed of at least three pyrite–matrix or pyrite-only zones. The core (Py2) is depleted in most trace elements. The intermediate zone (Py3) contains more Co, Ni, Cu, As, Sb, Tl, and Pb than the core, but these trace elements (except Pb) are mostly concentrated in the outmost rim (Py4). Lead is mostly concentrated in the intermediate zone. Gold, Ag, and Hg are only concentrated in the outmost rim. The zonation of Au is narrower than those of Co, Ni, As, Sb and Tl.

reduced S and Au is principally transported by HS^- ligands in the form of $Au(HS)^0$ and/or $Au(HS)_2^-$ complexes (Seward, 1973; Williams-Jones et al., 2009), the S isotopes can provide insights into the potential Au source. In Nibao, the broad range of in situ $\delta^{34}S$ values (−53.3 to 114.8‰) for pre-ore pyrites is likely the result of bacterial reduction from marine sulfate during diagenesis in (semi-) open and sulfate-limited systems (Aharon and Fu, 2000; Machel, 2001; Shen et al., 2001; Hou et al., 2016; Hu et al., 2018; Xie et al., 2018b; Li et al., 2019). The relatively narrow variation in $\delta^{34}S$ values for ore pyrite could have resulted from either pre-ore pyrites in the sedimentary rocks or from a magmatic source (Hou et al., 2016; Xie et al., 2018b; Li et al., 2019). This uncertainty can be further resolved by the geochemical ratios of pyrite (Large et al., 2007, 2009; Gregory et al., 2015a, 2016; Steadman et al., 2015; Wang and Zhu, 2015). One of these ratios–the Co/Ni ratio is widely used to identify the origin of pyrite (Bralia et al., 1979; Campbell and Ethier, 1984; Bajwah et al., 1987; Gregory et al., 2015a). Generally, the Co/Ni values in sedimentary pyrite are < 2, with a mean value of 0.63. Hydrothermal (vein) pyrites have values > 1, and ranging from 1.17 to 5.00 (Gregory et al., 2015a; Hou et al, 2016). Gregory et al. (2017) further suggested that the Zn/Ni ratio in sedimentary

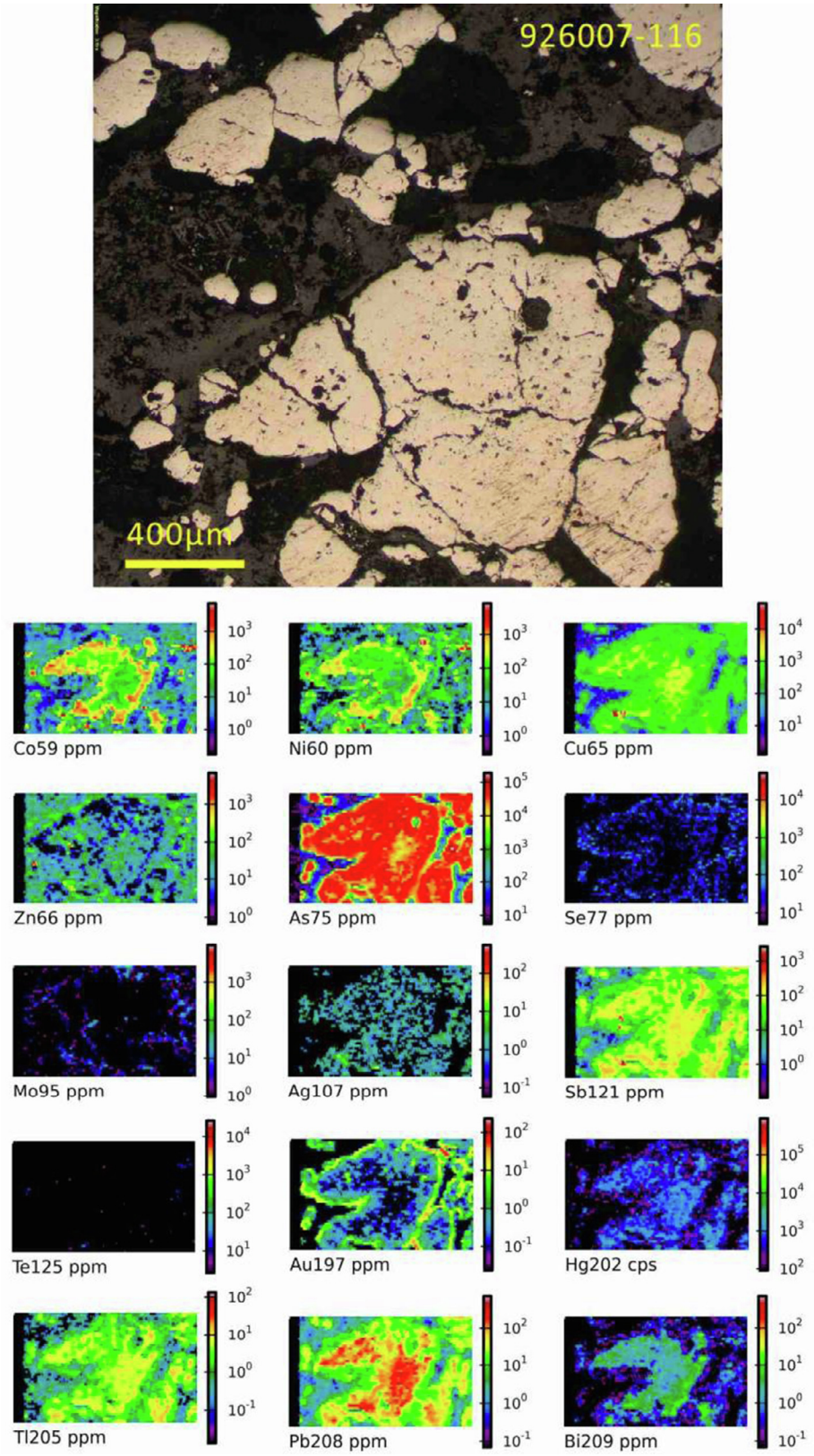

Fig. 10. Sample 942004-116 LA-ICP-MS trace element images. The core is depleted in Co, Ni, Au, and Bi. The intermediate zone (Py2) is relatively rich in Co, Ni, Cu, Sb, Tl, Pb, and Bi. The outmost rim (Py4) is especially rich in Au. Arsenic, Ag, and Hg are concentrated in this pyrite composite, but no clear zonation can be observed.

pyrite is mostly between 0.01 and 10. When examining the Co/Ni and Zn/Ni ratios in this study (Fig. 7E and F, respectively), most pyrites (regardless of type) had similar ratios, which mostly occur within or close to the range defined for sedimentary pyrite, although the textural evidence shows that Py3 and Py4 were formed during a hydrothermal stage. Additionally, the Co and Ni contents in all pyrites are positively correlated (R^2 = 0.71) (Fig. 7E). Taken together, this suggests that the ultimate source of trace elements in these pyrites (Py1–Py4) was

Table 4
Compilation of $\delta^{34}S$ isotope data (‰) of pyrites from the Nibao deposit.

Pyrite type	Min	Max	Median	Average
Py2 (this study; n = 9)	−4.69	−2.3	−3.48	−3.44
Py4 (This study; n = 9)	−5.26	−2.43	−3.36	−3.43
Pre-ore Py (Zheng, 2017; n = 14)	−5.35	13.4	−3.27	−0.43
Ore Py (Zheng, 2017; n = 17)	−5.24	8.48	−3.34	−2.33
Pre-ore Py (Li et al., 2019; n = 42)	−53.3	114.8	13.2	14.86
Ore Py (Li et al., 2019; n = 38)	−3.9	5.4	2.3	2.27
Pre-ore Py (Jin, 2017; n = 17)	−46.9	16.1	0.1	−2.43
Ore Py (Jin, 2017; n = 15)	−1.5	1.3	−0.1	−0.05

possibly the same. Therefore, a sedimentary S source for ore pyrite is more likely in Nibao. Furthermore, igneous rocks are rare in the region and the ages of the exposed (ultramafic and felsic dikes, ~77–99 Ma, Zhu et al., 2017) are clearly younger than the mineralization age of the Nibao deposit (~141 Ma, Chen et al., 2019), indicating that a magmatic source is unlikely in Nibao.

It has been demonstrated that the conversion (from pyrite to pyrrhotite) or destruction of early sedimentary pyrite can release trace elements, including Au and As (Large et al., 2011). Early enrichment of Au and As in source rocks (particularly in pyritic black shale) can be crucial to the formation of Carlin-type gold deposits (Gregory et al., 2015b). However, no evidence for wide–scale pyrite conversion and destruction has yet been found within either the Nibao deposit or the Youjiang Basin. Therefore, Au could not have been sourced directly from the sedimentary pyrite of the Permian sequences, the deepest strata revealed by present drill holes. However, from the Neoproterozoic to the Cambrian, the Yangtze Craton records several sequences of black shales in the basement of the Youjiang Basin, including the Neoproterozoic Duoshantuo Formation and the Lower Cambrian Niutitang Formation (Sahoo et al., 2016; Zhang et al., 2016; Gregory et al., 2017), although they are not exposed in the basin. The black shales in the Duoshantuo and Niutitang Formations are especially anomalous in terms of their trace element compositions, including As, Sb, Au, and Ag, and therefore have great potential as a source for the Au deposits.

7. Conclusions and problems remaining

In the Nibao deposit, pyrite is the major sulfide mineral, with minor amounts of arsenopyrite, sphalerite, realgar, orpiment, tennantite, and chalcopyrite. Four pyrite types (Py1–Py4) were identified based on textural and LA-ICP-MS analyses. Among them, only Py4—the overgrowth of pyrite rims and disseminated pyrite associated with arsenopyrite—contains economic concentrations of Au, and Au in Py4 is structurally bound (Au^{+}) within the pyrite lattice.

The $\delta^{34}S$ isotope ratios show that pre-ore pyrites have $\delta^{34}S$ values ranging broadly (−53.3 to 114.8‰), indicating that they were most likely generated via bacterial reduction from marine sulfates during diagenesis. The relatively narrow range of $\delta^{34}S$ values of ore pyrites, mostly varying from −5 to 5‰, indicates that S was derived either from sedimentary rocks or from a magmatic S source. Both the trace element ratio characteristics of the four pyrite types and the younger age of the igneous rocks in the region suggest a sedimentary source is more likely in Nibao.

The basement sequences of the Youjiang Basin, including the Neoproterozoic and Lower Cambrian black shales, are the most likely sedimentary sequences to have released Au from sedimentary pyrite. However, the mechanism for the release of Au is still unclear. Previous studies suggest that the release of Au from sedimentary sequences needs to be subjected greenschist-facies or higher grade metamorphism (Large et al., 2009, 2011; Wu et al., 2018). Currently there is no evidence showing that the Neoproterozoic and Cambrian sequences in the basement of the Youjiang Basin have been subjected to greenschist-facies or higher grade metamorphism. Ultimately, the results of our current study cannot definitively determine whether the sedimentary or magmatic source is correct. However, our analysis and the presence of black shale in the basement of the basin lead us to favor the sedimentary source.

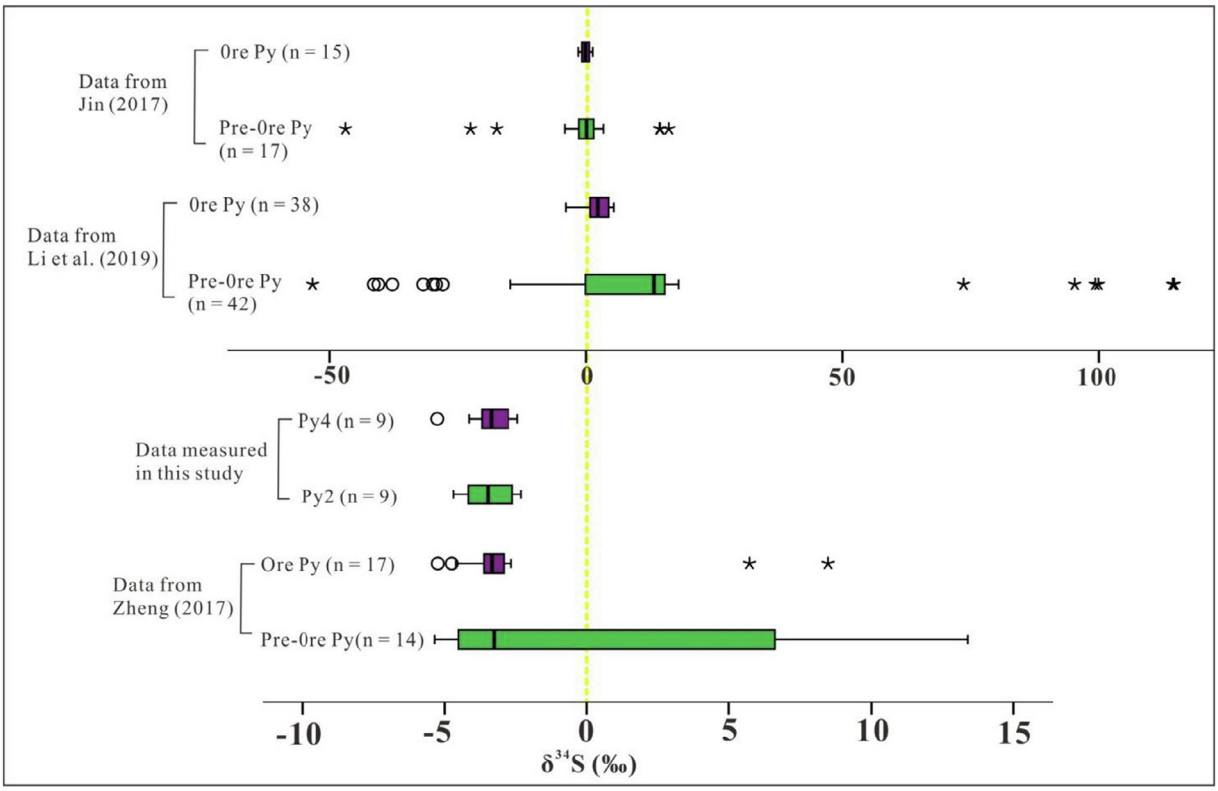

Fig. 11. Box plot of $\delta^{34}S$ isotope values of pyrites from the Nibao gold deposit (Data compiled from Jin (2017), Zheng (2017), Li et al. (2019); and this study).

Declaration of Competing Interest

The authors declare that they have no known competing financial interests or personal relationships that could have appeared to influence the work reported in this paper.

Acknowledgements

This work is supported by the National Key R&D Program of Deep Penetrating Geochemistry (grant 2016YFC0600607), National Natural Science Foundation of China (grant 41963004; 41703046), Guangxi Science and Technology Base and Talents Special Program (grant 2018AD19178), Scientific Research Foundation of Guilin University of Technology (grant RD18102807), Science and Technology Foundation of Guizhou Province (Qiankehejichu[2020]1Z034), and the Geological Research Project of Bureau of Geology and Mineral Exploration and Development Guizhou Province (Qian Di Kuang Ke He (2016) No. 12). We are grateful to the Geological Party 105, Guizhou Bureau of Geology and Mineral Exploration and Development for access to samples from the Nibao deposit. We thank Shijun Xia, Jianzhong Liu, Liansu Qi, Yingguo Zhang and Liangyi Xu for their guidance during sampling, and Leonid Danyushevsky, Karsten Goemann and Paul Olin for their assistance in petrographic investigations, SEM observations, and LA-ICP-MS analyses. We also thank the reviewers for their constructive comments and suggestions, which improved the final version of this manuscript.

Appendix A. Supplementary data

Supplementary data to this article can be found online at https://doi.org/10.1016/j.oregeorev.2020.103446.

References

Aharon, P., Fu, B.S., 2000. Microbial sulfate reduction rates and sulfur and oxygen isotope fractionations at oil and gas seeps in deepwater Gulf of Mexico. Geochim. Cosmochim. Acta 64, 233–246.
Bajwah, Z.U., Seccombe, P.K., Offlr, R., 1987. Trace element distribution Co: Ni ratios and genesis of the big Cadia iron copper deposit, New South Wales, Australia. Miner. Deposita 22, 292–300.
Basori, M.B.I., Gilbert, S., Large, R.R., Zaw, K., 2018. Textures and trace element composition of pyrite from the bukit botol volcanic-hosted massive sulphide deposit, peninsular malaysia. J. Asian Earth Sci. 158.
Bralia, A., Sabatini, G., Troja, F., 1979. A revaluation of the Co/Ni ration in pyrite as geochemical tool in ore genesis problems. Miner. Deposita 14, 353–374.
Cai, J.X., Zhang, K.J., 2009. A new model for the Indochina and South China collision during the Late Permian to the Middle Triassic. Tectonophysics 469, 35–45.
Campbell, F.A., Ethier, V.G., 1984. Nickel and cobalt in pyrrhotite and pyrite from the Faro and Sullivan orebodies. Can. Mineral 22, 503–506.
Chen, M., Bagas, L., Liao, X., Zhang, Z., Li, Q., 2019. Hydrothermal apatite SIMS ThPb dating: Constraints on the timing of low-temperature hydrothermal Au deposits in Nibao, SW China. Lithos 324–325, 418–428.
Chen, M.H., Mao, J.W., Bierlein, F.P., Norman, T., Uttley, P.J., 2011. Structural features and metallogenesis of the Carlin-type Jinfeng (Lannigou) gold deposit, Guizhou Province, China. Ore Geol. Rev. 43 (1), 217–234.
Chen, M.H., Mao, J.W., Li, C., Zhang, Z.Q., Dang, Y., 2015. Re-Os isochron ages for arsenopyrite from Carlin-like gold deposits in the Yunnan-Guizhou-Guangxi “golden triangle”, southwestern China. Ore Geol. Rev. 64, 316–327.
Cheng, Y.B., Mao, J.W., 2010. Age and geochemistry of granites in Gejiu area, Yunnan province, SW China: constraints on their petrogenesis and tectonic setting. Lithos 120, 258–276.
Cheng, Y.B., Mao, J.W., Spandler, C., 2013. Petrogenesis and geodynamic implications of the Gejiu igneous complex in the western Cathaysia block, South China. Lithos 175, 213–229.
Cline, J.S., Hofstra, A.A., 2000. Ore-fluid evolution at the Getchell Carlin-type gold deposit, Nevada, USA. Eur. J. Mineral 12 (1), 195–212.
Cline, J.S., Hofstra, A.H., Muntean, J.L., Tosdal, R.M., Hickey, K.A., 2005. Carlin-type gold deposits in Nevada: critical geologic characteristics and viable models. Econ. Geol. 100th Anniversary Volume, 451–484.
Cline, J.S., Muntean, J.L., Gu, X.X., Xia, Y., 2013. A comparison of Carlin-type gold deposits: Guizhou Province, golden triangle, southwest China, and northern Nevada, USA. Earth Sci. Front. 20 (1), 1–18.
Danyushevsky, L., Robinson, P., Gilbert, S., Norman, M., Large, R., McGoldrick, P., Shelley, M., 2011. Routine quantitative multi-element analysis of sulphide minerals by laser ablation ICP-MS: standard development and consideration of matrix effects. Geochem. Explor. Environ. A 11, 51–60.
Deditius, A.P., Utsunomiya, S., Renock, D., Ewing, R.C., Ramana, C.V., Becker, U., Kesler, S.E., 2008. A proposed new type of arsenian pyrite: composition, nanostructure and geological significance. Geochim. Cosmochim. Acta 72, 2919–2933.
Franchini, M., Mcfarlane, C., Maydagán, L., Reich, M., Lentz, D.R., Meinert, L., Bouhier, V., 2015. Trace metals in pyrite and marcasite from the Agua Rica porphyry-high sulfidation epithermal deposit, Catamarca, Argentina: textural features and metal zoning at the porphyry to epithermal transition. Ore Geol. Rev. 66, 366–387.
Frimmel, H.E., 2008. Earth’s continental crustal gold endowment. Earth Planet. Sci. Lett. 267 (1–2), 45–55.
Gao, Z.M., Li, H.Y., Yang, Z.S., Tao, Y., Luo, T.Y., Liu, X.F., Xia, Y., Rao, W.B., 2002. Metallogenic and Ore Prospecting of the Main Gold Deposits, Guizhou Province and Yunnan Province. Geological Publishing House, Beijing (in Chinese with English abstract).
Gilbert, S., Danyushevsky, L., Goemann, K., Death, D., 2014a. Fractionation of sulphur relative to iron during laser ablation-ICP-MS analyses of sulfie minerals: implications for quantifiation. J. Anal. At. Spectrom. 29, 1024–1033.
Gilbert, S., Danyushevsky, L., Rodemann, T., Shimizu, N., Gurenko, A., Meffre, S., Thomas, H., Large, R., Death, D., 2014b. Optimisation of laser parameters for the analysis of sulphur isotopes in sulfie minerals by laser ablation ICP-MS. J. Anal. At. Spectrom. 29, 1042–1051.
Gregory, D., Meffre, S., Large, R., 2014. Comparison of metal enrichment in pyrite framboids from a metal-enriched and metal-poor estuary. Am. Miner. 99, 633–644.
Gregory, D.D., Large, R.R., Halpin, J.A., Baturina, E.L., Lyons, T.W., Wu, S., Danyushevsky, L., Sack, P.J., Chappaz, A., Maslennikov, V.V., Bull, S.W., 2015a. Trace element content of sedimentary pyrite in Black Shales. Econ. Geol. 110, 1389–1410.
Gregory, D.D., Large, R.R., Halpin, J.A., Lounejeva, E., Wu, S., Bull, S.W., Sack, P.J., Lyons, T., Chappaz, A., 2015b. Accumulation of Trace Elements into Black Shale – How to Identify a Viable Source Rock for Orogenic and Carlin-style Gold Deposits. Pacrim, pp. 59–64.
Gregory, D.D., Large, R.R., Bath, A.B., Steadman, J.A., Wu, S., Danyushevsky, L., Bull, S.W., Holden, P., Ireland, T.R., 2016. Trace element content of pyrite from the Kapai Slate, St. Ives gold district, western Australia. Econ. Geol. 111, 1297–1320.
Gregory, D.D., Lyons, T.W., Large, R.R., Jiang, G., Stepanov, A.S., Diamond, C.W., Maria, F., Paul, O., 2017. Whole rock and discrete pyrite geochemistry as complementary tracers of ancient ocean chemistry: an example from the neoproterozoic doushantuo formation, china. Geochim. Cosmochim. Acta 216, 201–220.
Gu, X.X., Zhang, Y.M., Li, B.H., Dong, S.Y., Xue, C.J., Fu, S.H., 2012. Hydrocarbon- and ore-bearing basinal fluids: a possible link between gold mineralization and hydrocarbon accumulation in the Youjiang basin South China. Miner. Deposita 47, 663–682.
Guillong, M., Hametner, K., Reusser, E., Wilson, S.A., Günther, D., 2005. Preliminary characterisation of new glass reference materials (GSA-1G, GSC-1G, GSD-1G and GSE-1G) by laser ablation-inductively coupled plasma-mass spectrometry using 193 nm, 213 nm and 266 nm wavelengths. Geostand. Geoanal. Res. 29, 315–331.
Hou, L., Peng, H.J., Ding, J., Zhang, J.R., Zhu, S.B., Wu, S.Y., Wu, Y., Ouyang, H.G., 2016. Textures and in situ chemical and isotopic analyses of pyrite, Huijiabao Trend, Youjiang Basin, China: implications for paragenesis and source of sulfur. Econ. Geol. 111, 331–353.
Hu, R.Z., Su, W.C., Bi, X.W., Tu, G.Z., Hofstra, A.H., 2002. Geology and geochemistry of Carlin-type gold deposits in China. Miner. Deposita 37 (3–4), 378–392.
Hu, R.Z., Fu, S.L., Huang, Y., Zhou, M.F., Fu, S.H., Zhao, C.H., Wang, Y.J., Bi, X.W., Xiao, J.F., 2017. The giant South China Mesozoic low-temperature metallogenic domain: reviews and a new geodynamic model. J. Asian Earth Sci. 137, 9–34.
Hu, X.L., Gong, Y.J., Zeng, G.P., Wang, J., Yao, S.Z., 2018. Multistage pyrite in the Getang sediment-hosted disseminated gold deposit, southwestern Guizhou Province, China: insights from textures and in situ chemical and sulfur isotopic analyses. Ore Geol. Rev. 99, 1–16.
Jin, X.Y., 2017. Geology, Mineralization and Genesis of the Nibao, Shuiyindong and Yata gold deposits in SW Guizhou Province, China (Ph. D Thesis). China University of Geosciences, Wuhan, China (in Chinese with English abstract).
Large, R.R., Maslennikon, V.V., Robert, F., Danyushevsky, L.V., Chang, Z.S., 2007. Multistage sedimentary and metamorphic origin of pyrite and gold in the giant Sukhoi Log deposit, Lena gold province Russia. Econ. Geol. 102, 1233–1267.
Large, R.R., Danyushevsky, L., Hollit, C., Maslennikov, V., Meffre, S., Gilbert, S., Bull, S., Scott, R., Emsbo, P., Thomas, H., Singh, B., Foster, J., 2009. Gold and trace element zonation in pyrite using a laser imaging technique: implications for the timing of gold in orogenic and Carlin-style sediment-hosted deposits. Econ. Geol. 104, 635–668.
Large, R.R., Bull, S.W., Maslennikov, V.V., 2011. A carbonaceous sedimentary source-rock model for Carlin-type and orogenic gold deposits. Econ. Geol. 106, 331–358.
Li, C.P., Peters, S.G., 1999. Comparative Geology and Geochemistry of Sedimentary-rockhosted (Carlin-type) Gold Deposits in the People's Republic of China and in Nevada, USA (Master's Thesis). University of Nevada, Reno.
Li, J., Zhao, C., Huang, Y., Zhuo, Y., Li, J., 2019. In-situ sulfur isotope and trace element of pyrite constraints on the formation and evolution of the Nibao Carlin-type gold deposit in SW China. Acta Geochim. 38 (4), 555–575.
Li, S., Wang, D., Liang, T., Qu, W., Ying, L., 2008. Metallogenic epochs of the Damingshan tungsten deposit in Guangxi and its prospecting potential. Acta Geol. Sin. 82, 873–879 (in Chinese with English abstract).
Liu, J.Z., 2003. Ore characteristics and Au occurrence of the Shuiyindong Au deposit. Guizhou Geol. 20, 30–34 (in Chinese with English abstract).
Liu, J.Z., Deng, Y.M., Liu, C.Q., Xia, Y., Zhang, X.C., Tao, Y., 2006. Geochemical studies on the inclusion and isotopes of the Shuiyindong gold deposit. Guizhou Geol. 23, 51–56 (in Chinese with English abstract).
Liu, S., Su, W.C., Hu, R.Z., Feng, C.X., Gao, S., Coulson, I.M., Wang, T., Feng, G.Y., Tao, Y., Xia, Y., 2010. Geochronological and geochemical constraints on the petrogenesis of

alkaline ultramafic dykes from southwest Guizhou Province, SW China. Lithos 114 (1), 253–264.
Liu, Y., Hu, K., Han, S.C., Sun, Z.H., 2015. The nature of ore-forming fluids of the Carlintype gold deposit in southwest China: a case from the Zimudang gold deposit. Resour. Geol. 65, 136–159.
Love, L.G., 1971. Early diagenetic polyframboidal pyrite, primary and redeposited, from the Wenlockian Denbigh Grit Group, Conway, North Wales, U.K. J. Sediment. Petrol. 41, 1038–1044.
Machel, H.G., 2001. Bacterial and thermochemical sulfate reduction in diagenetic settings—old and new insights. Sedim. Geol. 140, 143–175.
Mao, J.W., Cheng, Y.B., Chen, M.H., Pirajno, F., 2013. Major types and time–space distribution of Mesozoic ore deposits in South China and their geodynamic settings. Miner. Deposita 48, 267–294.
Maslennikov, V.V., Maslennikova, S.P., Large, R.R., Danyushevsky, L.V., 2009. Study of trace element zonation in vent chimneys from the Silurian Yaman-Kasy VolcanicHosted massive sulfide deposit (Southern Urals, Russia) using laser ablationinductively coupled plasma mass spectrometry (LA-ICPMS). Econ. Geol. 104, 1111–1141.
Meffre, S., Large, R.R., Steadman, J.A., Gregory, D.D., Stepanov, A., Kamenetsky, V., Ehrig, K., Scott, R.J., 2015. Multi-stage enrichment processes for large gold-bearing ore deposits. Ore Geol. Rev. 76, 268–279.
Muntean, J.L., Cline, J.S., Simon, A.C., Longo, A.A., 2011. Magmatic–hydrothermal origin of Nevada's Carlin-type gold deposits. Nat. Geosci. 4 (2), 122–127.
Peng, Y.W., Gu, X.X., Zhang, Y.M., Liu, L., Wu, C.Y., Chen, S.Y., 2014. Ore-forming process of the Huijiabao gold district, southwestern Guizhou Province, China: evidence from fluid inclusions and stable isotopes. J. Asian Earth Sci. 93, 89–101.
Peters, S.G., Huang, J.Z., Li, Z.P., Jing, C.G., 2007. Sedimentary rock-hosted Au deposits of the Dian-Qian-Gui area, Guizhou, and Yunnan Provinces, and Guangxi District China. Ore Geol. Rev. 31, 170–204.
Pribil, M.J., Ridley, W.I., Emsbo, P., 2015. Sulfate and sulfie sulfur isotopes ($\delta^{34}S$ and $\delta^{33}S$) measured by solution and laser ablation MC-ICP-MS: an enhanced approach using external correction. Chem. Geol. 412, 99–106.
Qi, L.S., He, Y.N., Qi, J., Yang, T.C., Zhang, M.M., Zheng, Y., Zhang, C., 2014. New cognizance of orebody type and formation mechanism of Nibao gold deposit in Guizhou. Guizhou Geol. 31, 109–115 (in Chinese with English abstract).
Qin, J.H., Wu, Y.L., Yan, Y.J., Zhu, Z.F., 1996. Hercynian-Indonesian sedimentary tectonic evolution of the Napanjiang basin. Acta Geol. Sin. 70, 99–107 (In Chinese with English asbtract).
Reich, M., Kesler, S.E., Utsunomiya, S., Palenik, C.S., Chryssoulis, S.L., Ewing, R.C., 2005. Solubility of gold in arsenian pyrite. Geochim. Cosmochim. 69, 2781–2796.
Sahoo, S., Planavsky, N., Jiang, G., Kendall, B., Owens, J., Wang, X., Shi, X., Anbar, A., Lynons, T., 2016. Oceanic oxygenation events in the anoxic Ediacaran ocean. Geobiology.
Scott, R.J., Meffre, S., Woodhead, J., Gilbert, S.E., Berry, R.F., Emsbo, P., 2009. Development of framboidal pyrite during diagenesis, low-grade regional metamorphism, and hydrothermal alteration. Econ. Geol. 104, 1143–1168.
Seward, T.M., 1973. Thio-complexes of gold in hydrothermal ore solutions. Geochim. Cosmochim. Ac. 37, 379–399.
Shen, Y.N., Buick, R., Canfeld, D.E., 2001. Isotopic evidence for microbial sulphate reduction in the Early Archaean era. Nature 410, 77–81.
Simon, G., Kesler, S.E., Chryssoulis, S., 1999. Geochemistry and textures of gold-bearing Arsenian pyrite, Twin Creeks, Nevada: implications for deposition of gold in Carlintype deposits. Econ. Geol. 94, 405–421.
Steadman, J.A., Large, R.R., Meffre, S., Bull, S.W., 2013. Age, origin and significance of nodular sulfides in 2680 Ma carbonaceous black shale of the Eastern Goldfields Superterrane, Yilgarn Craton, Western Australia. Precambrian Res. 230, 227–247.
Steadman, J.A., Large, R.R., Meffre, S., Olin, P.H., Danyushevsky, L.V., Gregory, D.D., Belousov, I., Lounejeva, E., Ireland, T.R., Holden, P., 2015. Synsedimentary to early diagenetic gold in black shale-hosted pyrite nodules at the Golden Mile Deposit, Kalgoorlie, western Australia. Econ. Geol. 110, 1157–1191.
Steadman, J.A., Large, R.R., 2016. Synsedimentary, diagenetic, and metamorphic pyrite, pyrrhotite, and marcasite at the homestake BIF-hosted gold deposit, South Dakota, USA: insights on Au-As ore genesis from textural and LA-ICP-MS trace element studies. Econ. Geol. 111, 1731–1752.
Su, W.C., Dong, W.D., Zhang, X.C., Shen, N.P., Hu, R.Z., Hofstra, A.H., Cheng, L.Z., Xia, Y., Yang, K.Y., 2018. Carlin-type gold deposits in the Dian-Qian-Gui “Golden Triangle” of Southwest China. Rev. Econ. Geol. 20, 157–185.
Su, W.C., Xia, B., Zhang, H.T., Zhang, X.C., Hu, R.Z., 2008. Visible gold in arsenian pyrite at the Shuiyindong Carlin-type gold deposit, Guizhou, China: implications for the environment and processes of ore formation. Ore Geol. Rev. 33 (3), 667–679.
Su, W.C., Heinrich, C.A., Pettke, T., Zhang, X.C., Hu, R.Z., Xia, B., 2009. Sediment-hosted gold deposits in Guizhou, China: products of wall-rock sulfidation by deep crustal fluids. Econ. Geol. 104, 73–93.
Su, W.C., Zhang, H.T., Hu, R.Z., Ge, X., Xia, B., Chen, Y.Y., Zhu, C., 2012. Mineralogy and geochemistry of gold-bearing arsenian pyrite from the Shuiyindong Carlin-type gold deposit, Guizhou, China: implications for gold depositional processes. Miner. Deposita 47 (6), 653–662.
Tan, Q.P., Xia, Y., Xie, Z.J., Yan, J., 2015. Migration paths and precipitation mechanisms of ore-forming fluids at the Shuiyindong Carlin-type gold deposit, Guizhou China. Ore Geol. Rev. 69, 140–156.
Tan, Q., Xia, Y., Xie, Z., Wang, Z., Wei, D., Zhao, Y., Yan, J., Li, S., 2019. Two Hydrothermal events at the Shuiyindong carlin-type gold deposit in Southwestern China: insight from Sm–Nd dating of fluorite and calcite. Mineral 9 (4), 230.
Tu, G., 1992. Some problems onprospecting of super large gold deposits (in Chinese). Acta Geol. Sichuan Spec Issue 12, 1–9.
Wang, D.H., Chen, Y.C., Chen, W., Sang, H.Q., Li, H.Q., Lu, Y.F., Chen, K.L., Lin, Z.M., 2004. Dating of the Dachang superlarge tin-polymetallic deposit in Guangxi and its implication for the genesis of the No. 100 orebody. Acta Geol. Sin. (English Ed.) 78, 452–458.
Wang, L., Zhu, Y.F., 2015. Multi-stage pyrite and hydrothermal mineral assemblage of the Hatu gold district (west Junggar, Xinjiang, NW China): implications for metallogenic evolution. Ore Geol. Rev. 69, 243–267.
Wang, Z.P., Xia, Y., Song, X.Y., Liu, J.Z., Yang, C.F., Yan, B.W., 2013. Study on the evolution of ore-formation fluids for Au–Sb ore deposits and the mechanism of Au–Sb paragenesis and differentiation in the southwestern part of Guizhou Province, China. Chin. J. Geochem. 32 (1), 56–68.
Wei, D.T., Xia, Y., Tan, Q.P., Xie, Z.J., Yan, J., Guo, H.Y., Liu, J.Z., 2016. Comparative study of the wallrock and ore and ore forming mechanisms at the Nibao gold deposit, Guizhou. China. Acta Petrol. Sin. 32, 3343–3359 (In Chinese with English asbtract).
Williams-Jones, A.E., Bowell, R.J., Migdisov, A.A., 2009. Gold in solution. Elements 5, 281–287.
Wilkin, R.T., Barnes, H.L., 1997. Formation process of framboidal pyrite. Geochim. Cosmochim. Acta 61, 323–339.
Wu, Y.-F., Li, J.-W., Evans, K., Koenig, A.E., Li, Z.-K., O'Brien, H., Lahaye, Y., Rempel, K., Hu, S.-Y., Zhang, Z.P., Yu, J.-P., 2018. Ore-forming processes of the Daqiao Epizonal orogenic gold deposit, West Qinling Orogen, China: constraints from textures, trace elements, and sulfur isotopes of pyrite and marcasite, and Raman spectroscopy of carbonaceous material. Econ. Geol. 113 (5), 1093–1132.
Xia, Y., 2005. Characteristics and Model for Shuiyindong Gold Deposit in Southwestern Guizhou, China. (Unpublished Ph. D Thesis). Institute of Geochemistry, Chinese Academy of Sciences, Guizhou, China (in Chinese with English abstract).
Xia, Y., Zhang, Y., Su, W.C., Tao, Y., Zhang, X.C., Liu, J.Z., Deng, Y.M., 2009. Metallogenic model and prognosis of the Shuiyindong super-large stratabound Carlin-type gold deposit, Southwestern Guizhou Province, China. Acta Geol. Sin. 83, 1473–1482 (in Chinese with English abstract).
Xie, Z.J., Xia, Y., Cline, J.S., Koenig, A., Wei, D.T., Tan, Q.P., Wang, Z.P., 2018a. Are there carlin-type gold deposits in China? A comparison of the Guizhou, China, deposits with Nevada, USA deposits. Rev. Econ. Geol. 20, 187–233.
Xie, Z.J., Xia, Y., Cline, J.S., Pribil, M.J., Koenig, A., Tan, Q.P., Wei, D.T., Wang, Z.P., Yan, J., 2018b. Magmatic origin for sediment-hosted Au deposits, Guizhou Province, China: in situ chemistry and sulfur isotope composition of pyrites, Shuiyindong and Jinfeng deposits. Econ. Geol. 113 (7), 1627–1652.
Xu, B., Jiang, S.-Y., Wang, R., Ma, L., Zhao, K.-D., Yan, X., 2015. Late cretaceous granites from the giant Dulong Sn-polymetallic ore district in Yunnan Province, South China: geochronology, geochemistry, mineral chemistry and Nd–Hf isotopic compositions. Lithos 218, 54–72.
Yang, J.H., Cawood, P.A., Du, Y.S., Huang, H., Hu, L.S., 2012. Detrital record of Indosinian mountain building in SW China: provenance of the Middle Triassic turbidites in the Youjiang Basin. Tectonophysics 574–575, 105–117.
Zeng, Y.F., Liu, W.J., Chen, H.D., Zheng, R.C., Zhang, J.Q., Li, X.Q., Jiang, T.C., 1995. Evolution of sedimentation and tectonics of the Youjiang composite basin, south China. Acta Geol. Sin. 69, 113–124 (in Chinese with English abstract).
Zhang, X.C., Spiro, B., Halls, C., Stanley, C.J., Yang, K.Y., 2003. Sediment-hosted disseminated gold deposits in Southwest Guizhou, PRC: their geological setting and origin in relation to mineralogical, fluid inclusion, and stable-isotope characteristics. Int. Geol. Rev. 45 (5), 407–470.
Zhang, Y., Xia, Y., Wang, Z., Yan, B., Fu, Z., Chen, M., 2010. REE and stable isotope geochemical characteristics of Bojitian gold deposit Guizhou Province. Earth Sci. Front. 17, 385–395 (in Chinese with English abstract).
Zhang, Y., Yan, D.P., Zhao, F., Li, X.T., Qiu, L., Zhang, Y.X., 2016. Stratigraphic sequences, abundance anomalies and occurrences of As, Sb, Au, Ag in the Lower Cambrian Niutitang Formation in Kaiyang Phosphate Mine area. Acta Petrol. Sin. 32, 3252–3268 (In Chinese with English asbtract).
Zheng, L.L., 2017. Mineralization Mechanism and Ore-forming Process of the Nibao Gold Deposit in Southwestern Guizhou, China (Ph.D. thesis). Guizhou University, Guiyang, China, pp. 141 (In Chinese with English abstract).
Zheng, L., Yang, R., Gao, J., Chen, J., Liu, J., 2016. In-situ sulfur isotope and trace element of pyrite constraints on the formation and evolution of the Nibao Carlin-type gold deposit in SW China. Ac. Geochim. 9 (108).
Zhu, J.J., Hu, R.Z., Richards, J.P., Bi, X.W., Stern, R., Lu, G., 2017. No genetic link between Late Cretaceous felsic dikes and Carlin-type Au deposits in the Youjiang basin, Southwest China. Ore Geol. Rev. 84, 328–337.